

Toward Bioinspired Wet Adhesives: Lessons from Assessing Surface Structures of the Suction Disc of Intertidal Clingfish

Jessica A. Sandoval,^{*} Jade Sommers, Karthik R. Peddireddy, Rae M. Robertson-Anderson, Michael T. Tolley, and Dimitri D. Deheyn^{*}



Cite This: <https://dx.doi.org/10.1021/acsami.0c10749>



Read Online

ACCESS |



Metrics & More



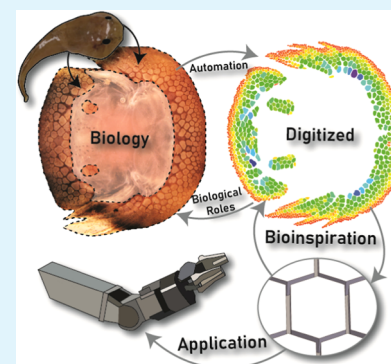
Article Recommendations



Supporting Information

ABSTRACT: The clingfish attaches to rough surfaces with considerable strength using an intricate suction disc, which displays complex surface geometries from structures called papillae. However, the exact role of these structures in adhesion is poorly understood. To investigate the relationship between papillae geometry and adhesive performance, we developed an image processing tool that analyzed the surface and structural complexity of papillae, which we then used to model hydrodynamic adhesion. Our tool allowed for the automated analysis of thousands of papillae in specimens across a range of body sizes. The results led us to identify spatial trends in papillae across the complex geometry of the suction disc and to establish fundamental structure–function relationships used in hydrodynamic adhesion. We found that the surface area of papillae changed within a suction disc and with fish size, but that the aspect ratios and channel width between papillae did not. Using a mathematical model, we found that the surface structures can adhere considerably when subjected to disturbances of moderate to high velocities. We concluded that a predominant role of the papillae is to leverage hydrodynamic adhesion and wet friction to reinforce the seal of the suction disc. Overall, the trends in papillae characteristics provided insights into bioinspired designs of surface microstructures for future applications in which adhesion is necessary to attach to diverse surfaces, in terrestrial or aquatic environments, even when subjected to disturbance forces of randomized directionality.

KEYWORDS: underwater adhesion, *Gobiesox maeandricus*, surface structuring, image processing, bioinspired design



INTRODUCTION

Adhesion involves highly complex and hierarchical structures in nature, and by understanding the biological intricacies of such adhesive structures, one can improve engineered adhesives.¹ The role of reversible adhesion in both the natural world and engineering is to temporarily bind to a surface, providing the opportunity to detach and re-attach as needed.^{1,2} In nature, animals use attachment to enhance their fitness, thereby taking advantage of beneficial opportunities, such as decreased instances of competition and predation or an increased abundance of resources, that would otherwise not be attained.³ In robotics, reversible adhesion enables improved manipulation⁴ and locomotion^{5,6} by managing contact at the interface between the robot and its environment. Adhesion can be broadly categorized into either dry (i.e., via van der Waals interactions⁷) or wet.⁸ Narrowing our focus to wet adhesion, this form of attachment takes advantage of viscous fluids, such as mucosal secretions (whether from terrestrial or aquatic organisms), found between an adhesive pad and a surface.⁹ Wet adhesion encompasses both capillarity,¹⁰ which is dependent on the surface tension of the fluid, and hydrodynamic forces.⁸ Hydrodynamic adhesion, also called Stefan adhesion, is due to viscous forces and is dependent on the rate at which an adhesive structure is pulled

from a surface.¹¹ Both capillarity and hydrodynamic adhesion are responsible for attachment in a variety of organisms, ranging from tree frogs^{9,12} to insects¹³ such as ants.¹⁴ The range of wet adhesive performances is related to the properties of the viscous fluids themselves, which have been found to be tunable in certain organisms. As demonstrated in the adhesives of spiders¹⁵ and bee pollen,¹⁶ humidity significantly influences its viscosity and subsequently its adhesive strength.

The performance of adhesives is dependent on surface properties (i.e., roughness and lubrication) and environmental conditions (i.e., wetness and disruptive forces).¹⁷ An increase in surface roughness has been demonstrated to greatly reduce attachment performance in synthetic adhesives.^{17,18} For instance, devices such as suction cups¹⁹ or microstructured adhesives¹⁸ function optimally on flat, smooth surfaces. Modifications to the geometries of the microstructured adhesives, such as the addition of hierarchical structures, can

Received: June 12, 2020

Accepted: September 10, 2020

Published: September 10, 2020

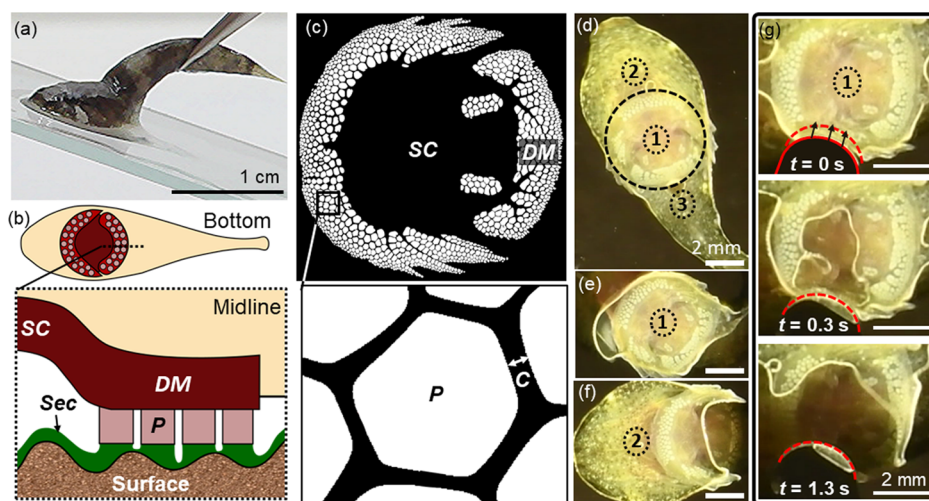


Figure 1. Visualization of the suction disc of the clingfish. (a) Image of the profile of a euthanized clingfish adhered to a glass surface. Scale bar, 1 cm. (b) Schematic of the ventral view of the clingfish. The suction disc is indicated in dark red. Inset: schematic of the midline view of a suction disc, illustrating the position and role of various components. The suction chamber (SC) forms a cavity of subambient pressure that is lined along its perimeter by a disc margin (DM), from which extend papillae (P). The papillae act to reinforce the disc margin on irregular surfaces and during large disruptive forces. Secretions (Sec) are released by the clingfish to coat the attachment surface. We propose that the secretions act to bridge the papillae to the surface. Schematics are not drawn to scale. (c) Binary image of the suction disc of the clingfish, for which only the papillae are shown. Inset: channels (C) form between papillae and are hypothesized to the channel fluid from the contact area of a papilla and thus aid in hydrodynamic adhesion. (d) Frustrated total internal reflection (FTIR) images for visualization of contact between a live clingfish and a flat surface. The imaging surface was transparent and wetted with salt water during the experiment. The clingfish was inverted during imaging, and the FTIR surface was imaged from above. Markers 1–3 denote the isolated chambers that we hypothesize are used to maintain subambient pressure. Chamber 1 is the suction disc (outlined by a dashed line). (e) Isolation of chamber 1 by using a blunt spatula to physically detach chambers 2 and 3 from the wetted surface. (f) Isolation of chamber 2 on the wetted surface. (g) Time series visualizing contact of the clingfish when the suction chamber was disrupted. Disruption occurred by a gentle prodding with a blunt spatula at the intersection of the pelvic and pectoral fins. Spatula, outlined with a solid red line, moved to the final position, denoted by the dashed red line.

64 have been shown to improve adhesive performance to rough
65 surfaces via enhanced surface conformation.²⁰

66 Attachment performance varies based on environmental
67 conditions.¹⁷ Wetness and humidity have been shown to
68 compromise adhesive performance due to the presence of
69 water between the contacting surfaces, excluding dry adhesives
70 from functioning in a wet domain.¹⁷ However, recent
71 developments to synthetic dry adhesives, including modifica-
72 tions to the material composition^{21,22} and structure, such as
73 the addition of cupped microstructures,²³ have conferred the
74 ability to adhere to wet surfaces. In addition to wetness, the
75 dislodgement forces per environment type also shape the
76 adhesive devices that can be applied.¹⁷ In a terrestrial
77 environment, gravity—of a predictable direction and magni-
78 tude—plays a substantial role in dislodgement. However, in a
79 wet environment, fluid flow—often of unpredictable direction
80 and magnitude—becomes a predominant mode of dislodge-
81 ment. Adhesive strategies to be employed underwater must be
82 resilient to these more randomized and dynamic disturbances.

83 The adhesive structures of biological organisms have
84 inspired engineers to develop new designs to improve
85 adhesion.^{1,24} In considering the methodology, previous work
86 in characterizing adhesive surface structures in biological
87 specimens has primarily involved observations and manual
88 quantification of often a small sample size.²⁵ Manual
89 quantification is a time-intensive process that quantifies a
90 relatively small percentage of adhesive structures across the
91 entire surface used in attachment by an organism. By
92 automating the analyses of surface patterns, we can more
93 efficiently quantify structures involved in adhesion to gain
94 insights that enable us to mimic their designs.

With inspiration from nature, engineers have developed a
95 range of bioinspired adhesives with impressive capabilities.³
96 For instance, the use of gecko-inspired, microstructured
97 adhesives has expanded robotic capabilities for applications
98 ranging from manipulating objects with irregular surface
99 topologies²⁶ and large objects in microgravity²⁷ to climbing
100 vertical walls.²⁸ Tree-frog-inspired surface structures have been
101 developed to enable the delicate manipulation of soft tissue
102 during surgery.²⁹ Remora-inspired adhesion has yielded
103 hitchhiking and manipulation capabilities for underwater
104 robots.^{30,31} In previous work, we have also developed a
105 synthetic suction disc inspired by the clingfish with improved
106 adhesion to various shapes and surface roughnesses.³²
107 However, the hierarchical mechanisms of adhesion for
108 application to clingfish bioinspired suction discs remained
109 relatively unexplored.
110

Echinoderms,³³ octopuses,^{34,35} and abalone³⁶ are just a few
111 examples of organisms that have been investigated for their
112 approaches to reversibly adhere to submerged surfaces.
113 Furthermore, fish, such as the remora,³⁷ cisorid catfish,^{38,39}
114 river loach,⁴⁰ and clingfish,^{19,41,42} have been studied for their
115 adhesive suction discs. The northern clingfish (*Gobiesox
116 maeandricus*) has become an impressive candidate for
117 bioinspired adhesion due to its ability to adhere to rough
118 surfaces while supporting large loads, up to 230 times its body
119 weight.¹⁹ Euthanized specimens have been reported to adhere
120 with an adhesive stress of approximately 40 kPa against coarse
121 (grain size, 269 μm) surface textures.⁴² These impressive
122 abilities make the clingfish an ideal candidate for identifying
123 designs to produce high-performance bioinspired adhesives.
124

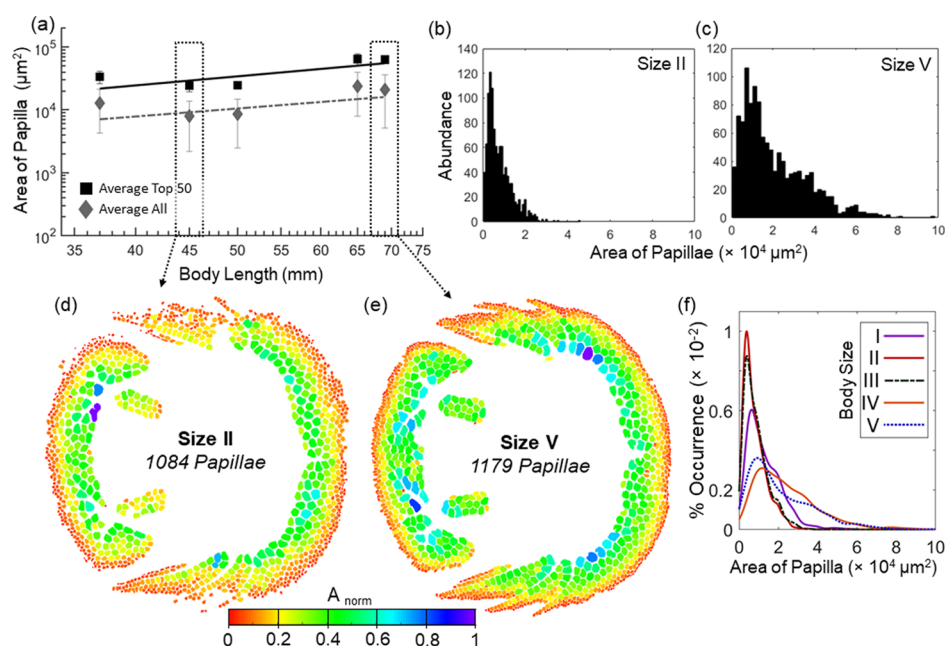


Figure 2. Characterizing the surface area of individual papillae across the suction disc. (a) Power-law relationship of the surface area (μm^2) of all papillae ($n = 4850$; gray diamond) and the 50 largest papillae ($n = 250$; black square) to the length of the clingfish body (mm), represented on a double-logarithmic plot. (b) Abundance of papillae with respect to the surface area, for size II. (c) Abundance of papillae with respect to the surface area, for size V. (d) Map for size II of the distribution of 1084 papillae based on the area normalized by the largest papillae (A_{norm}). (e) Map for size V of the distribution of 1179 papillae based on A_{norm} . (f) Kernel probability distributions of surface areas of papillae across all five clingfish body sizes (I–V).

125 The ability of the clingfish to attach to rough surfaces stems
 126 from its highly evolved suction disc formed by its modified
 127 pelvic and pectoral fins.⁴¹ The suction disc forms a cavity,
 128 considered the suction chamber (SC), and is lined by a disc
 129 margin (DM) (Figure 1b). The suction chamber maintains
 130 subambient pressure, while the disc margin acts to secure and
 131 seal its perimeter. A prominent feature of the disc margin is an
 132 extensive layer of papillae (P), which are geometric, flattened
 133 epithelial protrusions (Figure 1c). In this study, we focus on
 134 clarifying the role of papillae in adhesion.

135 Papillae have been the subject of only limited studies on
 136 their potential role in sealing the suction chamber.⁴² Previous
 137 work has proposed that the papillae leverage viscous forces that
 138 can be used to oppose axial disturbances, thereby securing the
 139 perimeter of the disc to the surface.¹⁹ The papillae act to
 140 reinforce the disc margin on irregular surfaces, in part by
 141 resisting shear and axial dislodgement forces. The papillae
 142 come in a diversity of sizes, shapes, and distributions across the
 143 suction disc, which had yet to be thoroughly characterized and
 144 quantified. By understanding the surface patterns of papillae
 145 across the disc, we aim to gain a clearer understanding of their
 146 added role in adhesion and to approximate their structure in a
 147 biomimetic analogue.

148 To complete this objective, we developed an approach based
 149 on image processing software to assess structural complexity in
 150 the suction discs of clingfish. This technique employed image
 151 processing algorithms used in computer science applications,
 152 ranging from fingerprint matching to vehicle traffic monitor-
 153 ing,⁴³ to understand the attributes and extent of the geometric
 154 biological structures involved in adhesion. We automated the
 155 characterization and quantification of papillae, which provided
 156 us with a more complete picture of their geometric
 157 characteristics within a given suction disc and across different
 158 sizes of suction discs. We used these results to model the

159 impact of the papillae on adhesion due to viscous forces. With
 160 the results of the geometric characterizations, we also
 161 computed the average shape and size of the papillae, which
 162 we then used to design and fabricate biomimetic surface
 163 textures. Ultimately, a profound understanding of the inherent
 164 complexity—i.e., shapes, sizes, distribution—of papillae would
 165 serve to inspire future biomimetic designs of high-performance
 166 wet adhesive devices.

167 ■ RESULTS

168 Our analyses combined experimental measurements with
 169 image processing techniques and modeling to address the
 170 role of papillae in biological adhesion. Our analysis across size
 171 in the clingfish highlighted key geometries of the adhesive
 172 structures, which we found to be shared by other organisms in
 173 the animal kingdom. The geometry of the papillae helps to
 174 leverage hydrodynamic forces for rate-dependent adhesion,
 175 which would be crucial in the turbulent intertidal habitat of the
 176 clingfish. Accordingly, we have replicated these structures in an
 177 artificial surface texture and experimentally validated their
 178 importance to resisting shear forces.

179 **Visualizing Complex Surface Structures of Live**
 180 **Specimen.** We imaged a live clingfish specimen on an
 181 inverted surface using frustrated total internal reflection
 182 (FTIR)⁴⁴ contact measurement to visualize the components
 183 of the fish involved with adhering to a surface (Figure 1b). We
 184 observed the formation of three distinctive chambers in which
 185 a pressure differential was formed (Figure 1d–f). The chamber
 186 of the suction disc (1) was formed by the union of the
 187 modified pelvic and pectoral fins. Two additional cavities
 188 formed anterior (2) and posterior (3) to the suction disc. We
 189 successfully isolated two of the three cavities involved with
 190 providing some contribution of suction (Figure 1e,f). Although
 191 the suction disc (1) is considered the main attachment organ

192 of the clingfish, we hypothesize that the two auxiliary cavities
193 formed anterior and posterior of the suction disc may provide a
194 supplemental contribution to adhesion via suction.

195 We disrupted the seal of the suction disc by gently prodding
196 the intersection of the pelvic and pectoral fins (Figure 1g),
197 referred to in previous work as a “vent”.⁴¹ When we disrupted
198 the suction chamber ($t = 0$ s), the disc remained adhered using
199 other modes of adhesion that therefore excluded suction. As
200 the disc margin detached from the surface ($t > 0.3$ s), the
201 papillae were the last in contact with the imaging plane. The
202 fish specimen detached itself by peeling its body laterally from
203 the surface. Overall, the ability of the papillae to remain
204 attached to the imaging surface after suction was removed
205 suggested additional adhesive capabilities associated with the
206 papillae, supplementary to sealing the suction chamber.

207 **Suction Disc Diameter Correlates to Body Size.** We
208 conducted our study of suction disc morphologies across five
209 preserved specimens (*G. maeandricus*) of different sizes,
210 denoted as sizes I–V, ordered by increasing body size. The
211 specimens ranged from a body length of 37 mm (size I; 0.54 g,
212 weight) to 69 mm (size V; 4.29 g, weight) (Table S1). The
213 diameter of the suction disc linearly corresponded to both
214 body size and weight of the clingfish (Figure S1a).

215 The total count of papillae per specimen exhibited a positive
216 correlation with body length (Figure S1b). The fewest number
217 of papillae, which totaled 800, was counted for the smallest
218 specimen (size I). The greatest number of papillae, 1179, was
219 counted for the largest specimen (size V). The quality of
220 preservation varied across specimens, leading to a limited
221 uncertainty on the count of papillae (this uncertainty was
222 estimated to <7% based on the extent of damaged areas; Figure
223 S1c,d).

224 **Surface Area of Papillae Scales with Body Size.** We
225 investigated the influence of body size on the surface area of an
226 individual papilla (Figure 2a). The average area of an
227 individual papilla increased from $(1.27 \pm 0.85) \times 10^4 \mu\text{m}^2$
228 for the smallest specimen (size I, $n = 800$ papillae) to $(2.08 \pm$
229 $1.56) \times 10^4 \mu\text{m}^2$ (size V, $n = 1179$ papillae; Table S2). We
230 modeled the power-law relationship between the surface area
231 of an individual papilla (A) and body length (l), with a scaling
232 exponent (m) and constant (k)⁴⁵

$$233 \quad A = k \cdot l^m \quad (1)$$

234 To calculate the scaling exponent and constant, we log-
235 transformed the data and performed a linear regression

$$236 \quad \log(A) = m \log(l) + \log(k) \quad (2)$$

237 We determined that the relationship between the surface area
238 of a papilla and body length was defined by a scaling exponent
239 of 1.3, when considering data from all papillae across all
240 specimens (Figure 2a; $n = 4850$; $p = 0.13$; r^2 -value, 0.60).
241 Given the large variability in the surface areas across the
242 entirety of the suction disc, we also quantified this trend
243 considering only the 50 largest papillae of each individual
244 (Figure 2a). We observed a more defined relationship between
245 the body length and surface area of the 50 largest papillae, with
246 a scaling exponent of 1.5 ($n = 250$; $p < 0.05$; r^2 -value, 0.81).
247 The scaling exponent between 1.3 and 1.5 signified that the
248 body size has a positive, nonlinear effect on the size of the
249 papillae.

250 Other groups of clingfish, such as the much larger Chilean
251 clingfish (*Sicyases sanguineus*), demonstrated a similar relation-
252 ship with body size and surface area. For instance, in samples

of preserved Chilean clingfish (body length, 29.4 cm; disc 253
diameter, 11.6 cm), the papillae measured to surface areas of 254
roughly $(1.9\text{--}3.0) \times 10^7 \mu\text{m}^2$, 2 orders of magnitude greater 255
than the papillae of *G. maeandricus* (Figure S3). 256

Surface Area of Papillae Decreases Radially. We 257
analyzed the distributions of papillae based on the surface 258
area across the entirety of each suction disc (Figure 2b,c). We 259
observed that the distributions of surface area exhibited a right- 260
skewed asymmetry and thus a larger concentration of smaller 261
papillae across every size of the suction disc (Figures S2 and 262
2b,c). The Kernel probability distributions of the surface area 263
also showed a right-skewed asymmetry across all body sizes 264
(Figure 2f). Therefore, the suction disc of the clingfish favors a 265
larger density of smaller papillae, and this trend is independent 266
of body size. 267

To understand the spatial distribution of papillae based on 268
area, we normalized (A_{norm}) the surface area of an individual 269
papilla (A_i) to that of the largest papilla (A_{max}) for each suction 270
disc ($A_{\text{norm}} = A_i/A_{\text{max}}$). We chose to normalize the surface area 271
to elucidate trends in papillae distribution across different body 272
sizes (Figure S2). For each of the five suction discs, the 273
distribution of A_{norm} was mapped to a binary image,⁴³ which 274
was generated by isolating the papillae, or regions of interest, 275
from the original micrographs. To demonstrate spatial trends 276
across the range of body sizes, we showed representative 277
examples of small (size II) and large (size V) body sizes 278
(Figure 2d,e). 279

As demonstrated in sizes II and V, a clear trend existed in 280
the distribution of papillae when considering their surface area. 281
We observed a decrease in the surface areas of the papillae 282
when extending from the center of the disc along the radius to 283
the outermost perimeter. The largest papillae ($A_{\text{norm}} > 0.80$) 284
were found to be located along the innermost radius of the 285
anterior and posterior regions of the suction disc. Conversely, 286
the smallest papillae ($A_{\text{norm}} < 0.20$) were located consistently 287
along the outermost radius of the disc. On average, eight rows 288
of papillae were expressed in both the anterior and posterior 289
regions of the suction disc, irrespective of body size. The lateral 290
regions of the disc margin exhibited a greater concentration of 291
small papillae ($A_{\text{norm}} < 0.20$), with comparison to both anterior 292
and posterior regions. These trends were consistent across all 293
five body sizes of the clingfish specimen (Figure S2). 294

We sought to understand the probability density functions 295
of papillae based on location along the suction disc. We 296
segmented one suction disc (size V) based on region, 297
differentiating between the anterior, posterior, and lateral 298
components of the disc margin. Of the anterior and posterior, 299
we deconstructed the disc into the components of “inner” 300
(three rows, innermost radius) and “outer” (two rows, 301
outermost radius). We also isolated the lateral components 302
of the disc margin (Figure 3a,d–f). 303 f3

A total of 357, 184, and 408 papillae were counted for the 304
outer, inner, and lateral components, respectively. We 305
superimposed the Kernel probability distributions of the 306
isolated regions (Figure 3c). Similar to the heat maps, the 307
outermost regions contained the greatest abundance of small 308
papillae, with an average area of $(1.00 \pm 0.50) \times 10^4 \mu\text{m}^2$ 309
(Figure 3g). The innermost regions contained the greatest 310
abundance of large papillae, with an average area of $(4.27 \pm$ 311
 $1.40) \times 10^4 \mu\text{m}^2$ (Figure 3h). Along the radius, the papillae 312
increased in size roughly 4.2 times from the outermost to the 313
innermost rows. The distributions of size were symmetric for 314
both the inner and outer regions of the anterior and posterior 315

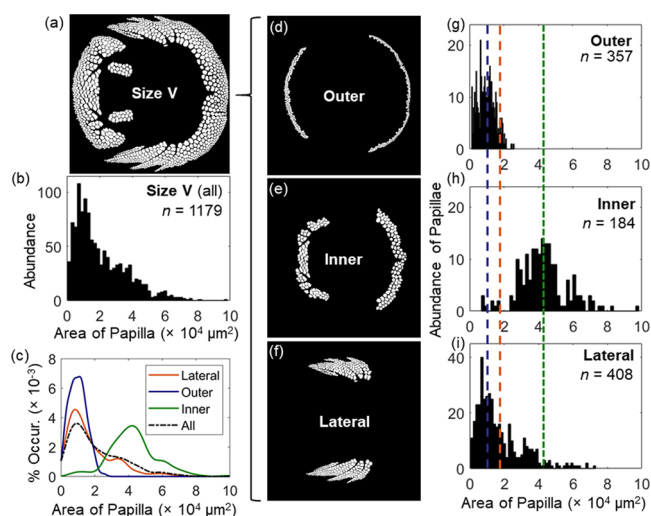


Figure 3. Segmentation of the suction disc for analysis of the spatial distribution of papillae based on size. (a) Binary image of the suction disc of size V. (b) Abundance of papillae based on surface area (μm^2). (c) Kernel probability distribution of the surface area of papillae (μm^2). Distributions of lateral components, orange; outer, blue; inner, green; and across all papillae of the suction disc, dashed black. (d) Binary image of the outer rows of the disc. (e) Binary image of the inner rows of the disc. (f) Binary image of lateral components. (g) Abundance of papillae based on the surface area for the outer disc margin. The mean is represented as the blue dashed line, centered at $1.00 \times 10^4 \mu\text{m}^2$. (h) Abundance of papillae based on the surface area for the inner disc margin. The mean is represented as the green dashed line, centered at $4.27 \times 10^4 \mu\text{m}^2$. (i) Abundance of papillae based on the surface area for lateral components. The mean is represented as the orange dashed line, centered at $1.74 \times 10^4 \mu\text{m}^2$.

disc margins (Figure 3c). Conversely, we observed a right-skewed asymmetry in the distribution of surface area for the

lateral fin regions, consistent with a greater, but non-homogeneous, concentration of small papillae (Figure 3i).

Aspect Ratio of Papillae Independent of Body Size.

We generated an image processing procedure to automatically calculate the aspect ratio across all papillae of the suction disc. The aspect ratio is a measure of the elongation of a papilla. To perform this calculation, our program automatically detected each papilla and drew the minimum bounding box around the region of interest (ROI) such that all sides and vertices were included. We then calculated the aspect ratio as the division of the longest side (l) of the bounding box by the shortest side (w , aspect ratio = l/w).

The average aspect ratio of the papilla was consistent across the body sizes, centered around 1.3 (Figure 4a). We therefore concluded that the aspect ratio of the papillae was independent of the body size of the clingfish. Comparing the specimen, the lowest average aspect ratio was calculated to be 1.25 ± 0.25 (size II, $n = 1084$), whereas the largest ratio was 1.37 ± 0.33 (size III, $n = 974$). To compare, a regular hexagon (RH) has an aspect ratio of 1.15. Therefore, we concluded that the papillae are elongated structures (Figure 4e), which are consistent across body sizes.

We then mapped the aspect ratio to the binary image of the suction disc for all body sizes. We noted a greater concentration of elongated papillae along the outer perimeter of the suction disc and along the lateral fin regions (Figures 4b and S4). Conversely, we observed less elongated papillae along the anterior, innermost region of the suction disc. Furthermore, we found a high abundance of elongated papillae at the innermost region of the posterior margin. The anterior and posterior papillae therefore exhibited divergent behaviors. Thus, the distribution of elongated papillae differed depending on the location along the suction disc.

The orientation of an elongated papilla was also dependent on its location (Figure 4b). The outermost papillae of the

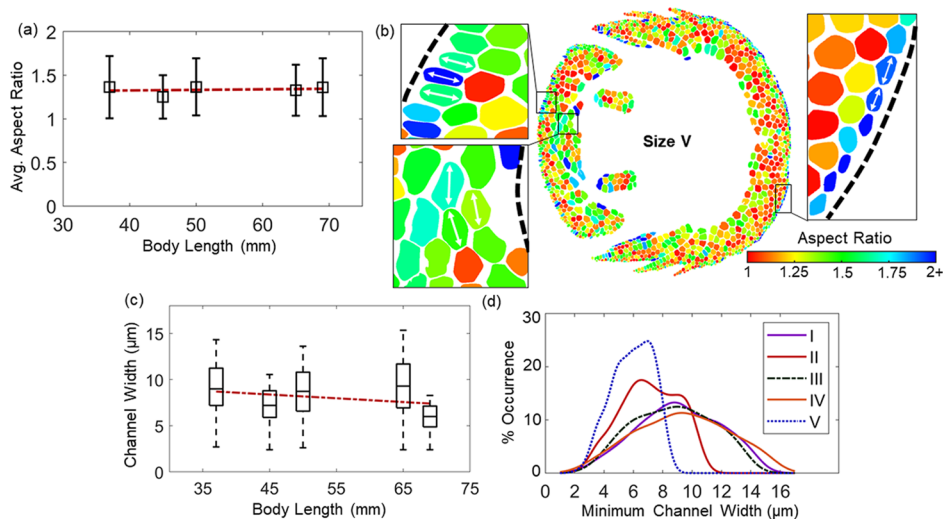


Figure 4. Characterizing aspect ratio and channel width to inform an idealized, average papilla. (a) Aspect ratio averaged across all papillae per specimen. Linear fit of data, red dashed line. All averages centered around a ratio of 1.3. (b) Aspect ratio mapped to the suction disc for size V. Aspect ratio ranges between 1 and 2. Inset, top left: papillae (aspect ratio >1.3) elongated anteroposteriorly along the outer posterior disc margin, indicated by arrows. Elongation perpendicular to the contour of the outer disc margin (dashed line). Inset, bottom left: papillae along the inner posterior disc margin elongated laterally, tangent to the contour of the inner disc margin (dashed line). Inset, right: papillae elongated laterally along the outer anterior disc margin, parallel to the contour of the outer disc margin (dashed line). (c) Box plot of the minimum channel width (μm) for all five body sizes. Linear fit of data (dashed red line; slope: -0.04 ; y-intercept: 10.2). (d) Kernel probability distributions of the minimum channel widths for body sizes I–V.

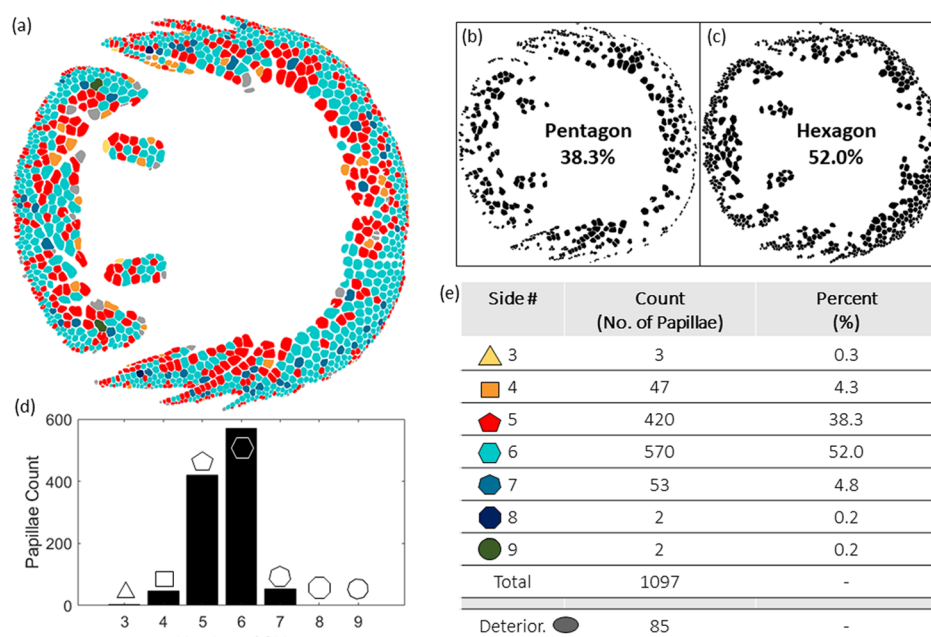


Figure 5. Geometric shape of papillae across the suction disc for size V. (a) Map of the distribution of papillae, based on the number of sides. Color coordination is as follows: three sides (light yellow), four sides (light orange), five sides (red), six sides (light turquoise), seven sides (navy blue), eight sides (dark blue), nine sides (dark green), and deteriorated (gray). (b) Binary image of only pentagonal papillae. (c) Binary image of only hexagonal papillae. (d) Abundance of papillae based on the number of sides. (e) Table detailing the abundance and percent occurrence of the different shapes. Papillae that were considered too deteriorated to be quantified for the number of sides are indicated by “deterior”.

anterior disc margin were elongated laterally, parallel to the contour of the outer disc margin. In contrast, the outermost papillae of the posterior disc margin were elongated anteroposteriorly, perpendicular to the contour of the outer disc margin. The innermost papillae of the posterior margin exhibited lateral elongation, tangent to the contour of the inner disc margin. The observations in elongation and orientations were consistent across body sizes (Figure S4). We hypothesize that the differences in orientations may play a role in reinforcing the perimeter of the suction chamber.

Channels between Papillae Direct Fluid from the Contact Area. We hypothesized that the channels between the papillae function to shuttle fluid from the contact area, thereby reducing the distance of separation and lowering the papillae to the surface. Previous work has demonstrated that microchannels surrounding surface structures used in wet adhesion channel fluid from beneath the biological adhesive pads, thus reducing the distance of separation between the epithelium to the surface on which the animal is attached.²⁹

To understand the microchannels used by the clingfish, we created a separate processing technique to calculate the minimum channel width between papillae. For this computation, we calculated for every pixel along the circumference of a papilla, the distance to its nearest neighboring papilla. We averaged across the five smallest distances per papilla to report the minimum distance to its neighbor, which we considered to be the minimum channel width. This computation was performed across the entirety of the suction disc, and the average per disc was then calculated.

We found that the minimum channel spacing between papillae was consistent and of the same order of magnitude, ranging between $9.1 \pm 2.7 \mu\text{m}$ (size I) and $5.9 \pm 1.3 \mu\text{m}$ (size V) for the smallest and largest body sizes, respectively (Figure 4c). The largest body size (V) exhibited the smallest average channel width, whereas the smallest body size (I) exhibited the

second largest channel width, resulting in a negatively sloped trend line (Figure 4c). The probability distributions of the channel width were symmetrical and did not exhibit skewness (Figure 4d).

We noticed that the channel width was affected by the degree of degradation of the specimen. A more degraded disc exhibited a loss of papillae along the outer perimeter, which by observation had narrower channels. Therefore, specimens, such as size V, that were better preserved generally had a smaller average channel spacing. Taking this into account, we concluded that overall the channel width was independent of body size and centered around an average spacing of $8.05 \mu\text{m}$ across the five specimens (Figure 4c).

Geometric Shape of Papilla Predominantly Hexagonal. We characterized the predominant shape of the papilla for the largest clingfish specimen (size V) and labeled a binary image by assigning colors to represent the number of sides of the structures (Figure 5a). We performed this task manually by referring to the original micrographs, where the number of sides was clearly delineated. The binary image, by contrast, exhibited smoothing of the vertices of the shapes, rendering subtle side lengths indistinguishable to automated image processing techniques.

Of the papillae in size V, we found that 52% were hexagonally shaped (Figure 5c,d). The second most abundant shape was pentagonal, representing 38.3% of all papillae (Figure 5b,d). The prevalence of other shapes fell considerably to 4.8 and 4.3% for heptagons and quadrilaterals, respectively (Figure 5e). We considered 85 of the papillae to be too deteriorated to yield a definitive conclusion on shape.

In the map detailing the distribution of shapes, higher concentrations of pentagons were found along the inner and outermost perimeters of the suction disc and also along the lateral fin rays (Figure 5a). Conversely, hexagonal structures were most prevalent, filling in the space between the inner and

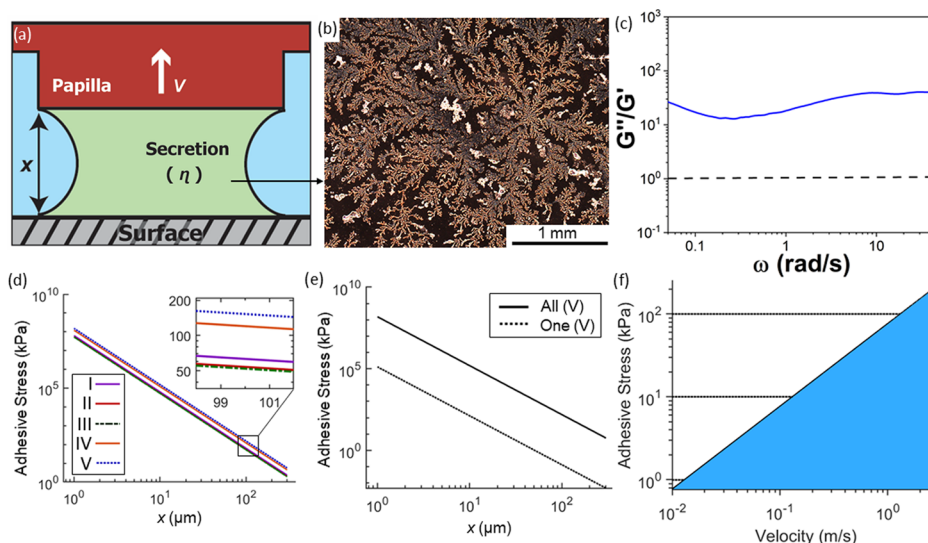


Figure 6. Modeling the contribution of papillae to Stefan adhesion. (a) Schematic representing the papillae as a parallel plate above a surface, separated by a distance (x). Secretions of viscosity (η) fill the spacing between the two faces. The papilla is pulled perpendicular to the surface with a velocity (V), which is representative of external disturbances. (b) Ferning pattern indicative of the mucosal content observed under microscopy of the secretion. (c) Ratio of the viscous modulus ($G''(\omega)$) to the elastic modulus ($G'(\omega)$), i.e., the loss tangent, of the isolated secretion. Secretion determined to be viscous as G''/G' is ~ 20 – 30 over the entire frequency range. (d) Double-logarithmic plot of the model of Stefan adhesion across a range of separation distances, for all five clingfish specimens. Velocity of disturbance, 2 m/s in simulation. Viscosity of secretion, 6.5 mPa·s. Total surface area per specimen was used to compute the adhesive stress. (e) Double-logarithmic plot of the model of Stefan adhesion for size V only. The adhesive stresses were modeled for one papilla of average surface area ($2.08 \times 10^4 \mu\text{m}^2$, “one”, dashed line) and across all papillae for size V (total, $2.46 \times 10^7 \mu\text{m}^2$, “all”, solid line). (f) Double-logarithmic plot modeling Stefan adhesion across all papillae for size V, varying the velocity of disturbance from 0 to 3 m/s. This range encompasses the fluid flow velocities that the clingfish is known to withstand in nature. Distance of separation: 100 μm . The shaded region indicates the contribution due to Stefan adhesion. The dotted line represents the adhesive stresses of 1, 10, and 100 kPa at 0.01, 0.13, and 1.31 m/s, respectively.

423 outer perimeters. We observed an appreciable presence of
424 shapes that have less than five sides or greater than six. We
425 suggest that the prevalence of such shapes aided with packing
426 the nonuniform surface of the disc margin of the clingfish.

427 **Characterization of the Secretion.** We investigated the
428 linear viscoelastic properties of the secretions found beneath
429 the suction disc (Figure 6a–c). As demonstrated using optical
430 microscopy, the secretions when dried crystallized into a
431 ferning pattern, indicative of a mucosal contribution to its
432 composition (Figure 6b).^{46,47} We performed passive micro-
433 rheological measurements of the clingfish secretion to
434 determine the elastic modulus ($G'(\omega)$), viscous modulus
435 ($G''(\omega)$), and viscosity. We found that the viscous modulus
436 was over an order of magnitude larger than the elastic modulus
437 at all explored frequencies (Figure 6c). This finding indicated
438 that the secretion behaves as a viscous, not viscoelastic, fluid at
439 nano- and microscales of interaction.⁴⁸ The viscosity of the
440 secretion was calculated to be 6.5 ± 1 mPa·s; by comparison,
441 the viscosity of water is 1 mPa·s. The value of viscosity
442 calculated from the microrheological experiments was then
443 used to model its impact on hydrodynamic adhesion across the
444 entirety of the suction disc.

445 **Modeling the Contribution of Hydrodynamic Adhe-**
446 **sion.** With an understanding of the geometric characteristics
447 of the papillae and microrheological properties of the secretion,
448 we estimated their contributions to hydrodynamic adhesion.
449 The secretions produced by live clingfish fill the space between
450 the papillae and a surface and would resist axial separation.
451 Hydrodynamic adhesion perpendicular to the surface (Stefan
452 adhesion, F_{Stef}) can be modeled for the case of two parallel,
453 rigid, circular plates of radius (r) separated from each other by
454 a distance (x) (Figure 6a).²⁵ A fluid layer of viscosity (η) fills

the space between the two plates, which separate with a 455
relative velocity ($V = dx/dt$). The resistance to separation is 456
the rate-dependent adhesive force. We generalized the 457
calculation of Stefan adhesion to eq 3 to consider the surface 458
area of the papilla (A), which accounted for noncircular surface 459
geometries²⁵ 460

$$F_{\text{Stef}} = \frac{3\pi r^4 \eta}{2x^3} \frac{\partial x}{\partial t} \approx \frac{3A^2 \eta}{2\pi x^3} \frac{\partial x}{\partial t} \quad (3) \quad 461$$

By eq 3, when pulled axially, Stefan adhesion is directly 462
proportional to the rate of the disturbance, viscosity of the 463
secretion, and surface area of the papillae. Adhesion is inversely 464
related to the distance of separation between a papilla and the 465
surface to which it is adhered. Therefore, by reducing the 466
distance of separation, the papillae can increase the 467
contribution of adhesion due to viscous forces. 468

Using eq 3, we modeled the influence of papillae on 469
adhesion, varying either their distance of separation or the 470
velocity of an axial disturbance. Adhesive stress (σ_{Stef}) was 471
calculated as the amount of resistance to separation due to 472
hydrodynamic forces (F_{Stef}) as a function of the contact surface 473
area (A) ($\sigma_{\text{Stef}} = F_{\text{Stef}}/A$). In the models, we set the viscosity of 474
the secretion to be 6.5 mPa·s, as determined from the 475
microrheological experiments. 476

We modeled how varying the distance of separation to a 477
surface impacted adhesion. We evaluated the adhesive stress 478
for a range of separation distances, varying from 1 to 300 μm . 479
We chose this range based on the previous literature in tree 480
frogs, which reported a distance of separation that varied 481
between 5 and 300 μm .¹² For this study, we also used a 482
velocity of disturbance of 2 m/s. We chose this velocity from 483

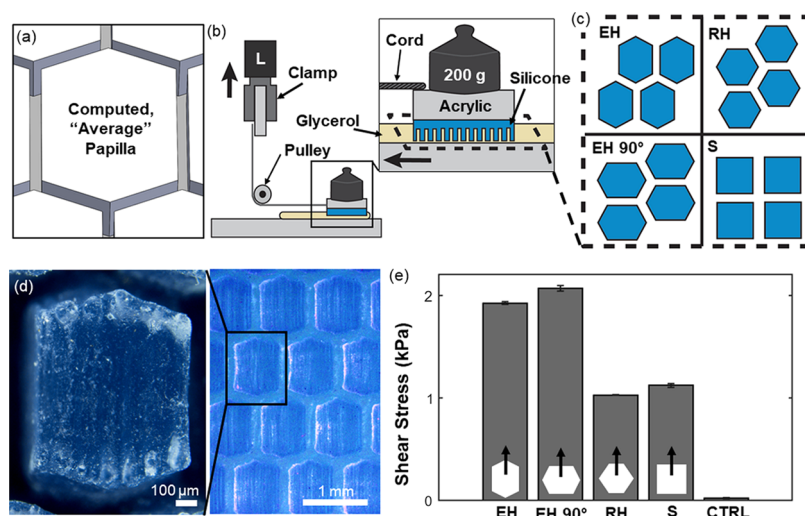


Figure 7. Experimentally validating the effect of the geometry of the surface patterns on resistance to shear disturbances. (a) Computer-generated rendering of an “average” papilla, based on the average shape, channel width, surface area, and aspect ratio. (b) Experimental setup to validate the effect of the surface structures on shear stress. The surface structures were composed of silicone (dyed in blue to ease visualization) that were then bonded to a stiff acrylic backing. An inextensible cord was applied to the acrylic backings and routed through a frictionless pulley to a clamp connected to a load cell of a universal testing machine. A preload of 200 g was applied to the backing. (c) Schematic of the patterns tested, consisting of either elongated hexagons (EHs), regular hexagons (RHs), elongated hexagons oriented orthogonal to the direction of motion (EH90), or squares (S). All structures were designed with the same surface area. (d) Biomimetic surface structure (EH). All structures were composed of silicone. Scale bar, 100 μm . Inset: scale bar, 1 mm. (e) Performance of the surface structures when pulled in shear on a glycerol-lubricated surface. Control was a silicone surface devoid of surface structures. All trials performed in triplicate.

484 an estimate of the forces experienced by the clingfish in its
 485 natural habitat.⁴⁹ The adhesive stresses across the five body
 486 sizes all exhibited exponential decay given an increasing
 487 distance of separation from the surface (Figure 6d). That is,
 488 the greater the distance to the surface, the less of a role the
 489 papillae have in adhesion. Additionally, the largest of the
 490 clingfish body sizes (V) was modeled to have between 2.5 and
 491 3 times greater adhesive stress than the smallest of body sizes
 492 (I, II).

493 We modeled the cumulative effect of papillae on adhesion
 494 for one specimen (size V; Figure 6e). The surface area of the
 495 single papilla, labeled as “one”, was the average surface area
 496 computed for size V, $2.08 \times 10^4 \mu\text{m}^2$. The total surface area of
 497 size V was calculated to be $2.46 \times 10^7 \mu\text{m}^2$. Adhesive stress
 498 across all of the papillae of size V was 3 orders of magnitude
 499 greater than that of a single papilla, hence the linear relation to
 500 area (Figure 6c). In high abundances, the papillae greatly
 501 increase their collective surface area, thereby increasing their
 502 impact on Stefan adhesion.

503 We modeled the impact of velocity on adhesion, given a
 504 disturbance acting perpendicularly on a clingfish (size V;
 505 Figure 6f). For this study, we fixed the distance of separation to
 506 100 μm , an intermediate value from our previously reported
 507 range. We modeled the range of axial velocities from 0 to 3 m/
 508 s. We chose this range since the body of a clingfish is projected
 509 to withstand disturbances between 2 and 3 m/s in the
 510 intertidal, while their habitat has registered wave surges up to 8
 511 m/s.⁴⁹ Turbulent fluid flow would result in an axial lift of the
 512 body of the clingfish. We approximated the axial velocity due
 513 to turbulence to be roughly equal to the velocity of the fluid in
 514 the environment.

515 Given that Stefan adhesion scales linearly with velocity, we
 516 found that flow velocities of 0.01, 0.13, and 1.31 m/s resulted
 517 in adhesive stresses on the order of 1, 10, and 100 kPa,
 518 respectively. We represented this linear relationship on a

519 logarithmic plot to emphasize the contribution of Stefan
 520 adhesion at velocities of different orders of magnitude. In sum,
 521 the velocity of an axial disturbance greatly influenced the
 522 adhesive stress achieved by the papillae. Stefan adhesion
 523 provided by the papillae would therefore be most beneficial in
 524 instances of disturbances of moderate to high velocities on the
 525 order of or greater than 0.1 m/s. The papillae could therefore
 526 act as a fail-safe to the suction disc, such that at higher vertical
 527 velocities of the clingfish due to a disturbance, the papillae
 528 would adhere with greater strength to a surface of the rocky
 529 intertidal. Adhesion of the papillae would ensure that the edge
 530 of the disc margin does not detach from its substrate, which
 531 would compromise the subambient pressure of the suction
 532 chamber.

Development of a Surface Pattern Mimicking the Papillae.
 533 We developed a biomimetic surface pattern to
 534 empirically test the effect of the geometry of the papillae when
 535 subjected to shear forces (Figure 7). From the results of the
 536 automated characterizations, we computed an “average”
 537 papilla, which resulted in an elongated hexagon (EH, aspect
 538 ratio, 1.3), which was consistent with the averages computed
 539 across all body sizes of clingfish (Figure 7a,d). The surface area
 540 of the individual biomimetic structure was designed to be equal
 541 to the average area of an individual papilla (size V), scaled by a
 542 factor of 10 (total surface area, 0.21 mm^2). The biomimetic
 543 surface pattern was compared to a pattern of regular hexagons
 544 (RHs) and a pattern of squares (S), both with the same surface
 545 area. We varied the orientation of the elongated hexagon, such
 546 that the hexagon was either oriented along (EH) or orthogonal
 547 to (EH90) the axis of elongation (Figure 7c). The control was
 548 devoid of surface structures. The surface patterns were
 549 composed of silicone and were pulled in shear along an acrylic
 550 surface lubricated with glycerol (viscosity, 1.4 Pa·s), which was
 551 used as an approximation of the secretions.
 552

553 We found that the averaged, biomimetic papillae (EH)
554 experienced the greatest shear stress, in comparison to all other
555 geometries. The biomimetic texture resulted in a shear stress
556 that was roughly twice that of either the regular hexagon or
557 square textures and 80 times that of the control. All surface
558 textures outperformed the control, demonstrating the need for
559 surface structuring to maintain attachment while subjected to
560 shear forces.

561 Additionally, the orientation of the elongated hexagon when
562 compared to the direction of motion only marginally impacted
563 the shear stress of the surface structure ((2.07 ± 0.03) – $(1.92$
564 $\pm 0.01)$ kPa for EH90 and EH, respectively). We therefore did
565 not notice an orientation preference of the biomimetic
566 structure.

567 These experimental results demonstrate the utility of surface
568 structures in resisting shear forces on lubricated surfaces. This
569 experiment also supports the conclusion that an elongation of a
570 surface structure best improves attachment performance.

571 ■ DISCUSSION

572 The suction disc of the clingfish is highly complex and employs
573 a variety of attachment processes at multiple scales to optimally
574 adhere to rough surfaces underwater. The papillae of the
575 clingfish that we examined exhibited distinctive morphological
576 trends (surface area, channel spacing, shape, and elongation),
577 most of which were independent of body size. In this work, we
578 highlighted the importance of the geometric arrangements and
579 characteristics of the papillae, which aided in attachment via
580 hydrodynamic adhesion. We concluded that these structures,
581 coupled with the properties of the secretions, have the
582 capabilities to reinforce the disc margin by preventing a leak
583 in the seal of the suction chamber. These surface structures are
584 therefore vital at resisting both axial and shear dislodgement
585 forces and are viable candidates for replication in biomimetic
586 analogues. We implemented an “averaged” papilla in a
587 biomimetic surface texture to experimentally validate our
588 hypotheses and demonstrate a potential use application.

589 **Geometric Shape Helps to Resist Shear Forces.** The
590 papillae of the clingfish were predominantly hexagonal,
591 followed by pentagonal, in shape. Theoretical models of
592 epithelial cell division to fill an irregular global shape found
593 that the distribution of epithelial cells converged to hexagonal
594 (46.4%), pentagonal (28.9%), and heptagonal (20.8%) when
595 driven by stochastic cell division alone.⁵⁰ The similarities in the
596 ratios of shapes between the theoretical model and the
597 clingfish may suggest a function of the shapes of the papillae.
598 Hexagons would be used to effectively pack of the surface,
599 while other shapes would be used to compensate for the
600 irregular topologies of the disc margin.⁵⁰

601 We have experimentally demonstrated that the shape of the
602 surface structure affected its resulting shear stress. Elongated
603 hexagons, of the same aspect ratio of the averaged papillae,
604 were the best-performing shape in shear. This finding is
605 consistent with previous work, in which textures with
606 elongated hexagonal shapes were found to increase the
607 coefficient of friction to wet surfaces in comparison to other
608 polygonal shapes.²⁹

609 We experimentally demonstrated that the orientation of the
610 elongated papillae did not significantly impact shear stress.
611 This finding contrasts with previous studies that have
612 demonstrated that sliding in the direction of elongation
613 improved the coefficient of friction of a surface structure.²⁹
614 Previous work attributed the orientation-dependent behavior

on the flow of fluid around the surface structures. Accordingly,
615 a greater amount of fluid was reported to be flushed onto the
616 contact area when sliding in the direction perpendicular to
617 elongation, thus reducing the coefficient of friction.²⁹ It is most
618 likely that the designs of our prototype and experiment may
619 have resulted in the contrasting behavior to previous work.
620 Indeed, our prototype was designed with channels that were
621 roughly 10 times greater than that of previous work, which may
622 have resulted in a much greater fluid channeling capacity.²⁹
623 Thus, it appears that the difference in the designs between our
624 study and the literature may have reduced the potential for
625 fluid to flush into the contact area during trials, resulting in the
626 reduced impact of orientation on shear stress. 627

The distribution of elongated hexagonal papillae could be
628 used to understand how to reinforce a disc margin when
629 confronted with shear loads from random directions. For
630 instance, the papillae of the outermost rows were greatly
631 elongated, spanning laterally for the front of the disc and
632 anteroposteriorly for the back. The elongations of papillae
633 along the outer rim of the disc margin, and their nonuniform
634 orientations, would act to counter shear loads from random,
635 nonuniform directions, which would prove particularly
636 beneficial for a clingfish given its rocky shoreline environment.
637 Lessons from the spatial arrangement of elongated papillae
638 could be used to inform the development of adhesive surface
639 textures that are resistant to randomized shear disturbances. 640

Previous work reported that from each papilla extends a
641 dense array of microscopic extracellular cuticle⁴¹ terminated
642 with nanofilaments at the tips.^{19,42} The cuticle was
643 hypothesized to spread and seal against surface asperities,
644 leading to an increased area of contact and coefficient of
645 friction.^{32,42} Although our study primarily focuses on how the
646 macroscopic geometries of the papillae affect adhesive
647 performance, these microscopic structures cannot be over-
648 looked in their contributions to resisting dislodgement via an
649 increased coefficient of friction. 650

Papillae Provide Crack Tolerance during Adhesion to
Rough Surfaces. We propose that structuring the surface of
652 the disc margin helps to make attachment to rough surfaces
653 feasible. The shape and spacing of papillae in the disc margin
654 resulted in an increased occurrence of fluid channeling through
655 a dense network of microchannels and greater conformation to
656 surface asperities. Fluid channeling could reduce the overall
657 distance of separation between the papillae and a surface.
658 Increased fluid channeling would therefore exponentially
659 increase the contribution of papillae to Stefan adhesion. The
660 presence of channels would also provide a form of geometric
661 compliance within the disc margin, such that it can better
662 adapt to rough surfaces and improve its seal. 663

Surface structuring would function to arrest cracks at the
664 interface of the suction disc and a surface, similar in function to
665 the segmented adhesive pads of other organisms, such as the
666 bush cricket.⁵¹ The structural discontinuities provided by the
667 papillae would prevent the propagation of a crack within the
668 seal of the disc margin that would otherwise compromise the
669 chamber of subambient pressure. We suggest that this function
670 partially explains the radial trend in the size of the papillae.
671 Specifically, the dominant presence of small papillae along the
672 outer perimeter of the disc margin would provide greater
673 instances of surface discontinuities that could be used to arrest
674 the propagation of cracks that begin around the outer rim of
675 the disc. We anticipate that this crack prevention mediated by
676 the arrangement of papillae is vital to successfully adhering to
677

rough surfaces in turbulent environments. We suggest that understanding such patterns in the spatial arrangements of papillae should be further considered while implementing the design of bioinspired surface structures, which could yield more versatile adhesion capabilities.

Rate-Dependent Adhesion for Turbulent Environments. The velocities of a disturbance common in an intertidal environment considerably influenced the resulting adhesive stress. We found that the adhesion of the papillae would be greatest during considerable disturbances, such as a wave surge, to which clingfish are routinely subjected in their natural habitat. Turbulent fluid flow would generate considerable lift of the body of the clingfish, resulting in a large, instantaneous load perpendicular to a surface. The wave-swept rocky habitats in which the clingfish resides register peak flow velocities from 5 to 8 m/s.⁴⁹ The individual bodies of the clingfish are expected to withstand flow velocities of 2–3 m/s, which encompasses both laminar and turbulent characteristics.⁴⁹ The chaotic water flow of the intertidal habitat therefore subjects the clingfish to a variety of external disturbances, which consist of high normal and shear loads from nonuniform directions.

Based on our analysis, we concluded that the adhesion of the suction disc of the clingfish was dependent on the environmental stimulus. In scenarios of low-frequency disturbances, this analysis indicates that suction would play the predominant role in attaching to surfaces. In conditions of high-frequency disturbances, our analysis leads us to conclude that both suction and hydrodynamic adhesion play critical, yet somewhat separate, roles in remaining attached to a substrate. Suction would provide significant adhesion against axial loads. Hydrodynamic adhesion would serve to reinforce the seal of the suction chamber. Maintaining the disc margin attached to a surface is therefore critical to the success of the suction chamber and adhesive disc as a whole. Considering that the potential for dislodgement is greatest during disruptive, high-frequency disturbances, the clingfish would need to employ multiple adhesion processes to secure attachment in variable and unpredictable environments.

One important consideration in experimentally evaluating the adhesive stress of the clingfish is the rate of dislodgement. Previous work measured the adhesive stress of clingfish at low rates of disturbance (0.017 m/s), yielding a tenacity of 29 kPa (smooth surface, unfouled).⁴² We hypothesize that the low linear velocity of the experimental setup would have rendered negligible the contribution of hydrodynamic forces to adhesion, and thus, the tenacity reported was predominantly due to suction. We would therefore suggest testing adhesion at a higher range of linear velocities to understand the effects of hydrodynamic adhesion in a biological specimen.

The model of Stefan adhesion used in this study served to understand the impact of surface structures on adhesion. This model, however, approximated the papillae as rigid, which observationally is not the case for the clingfish. An additional factor to consider in our model of hydrodynamic adhesion would be the material stiffness of the papillae.⁵² Our model of the adhesive stress would be impacted by the deformation of the papillae experienced when in contact with a surface. We recognize that there are also likely other types of forces involved in attachment, including viscous friction or potentially a nonzero contribution of van der Waals forces.¹² Therefore, our investigation into the adhesion of the suction disc primarily identifies and considers the role of predominant surface

structures in adhesion while subjected to disturbances of high velocities, thus likely underestimating the true performance of this highly complex adhesive disc.

Analytical Tools Advance Understanding of Complex Geometries. Our use of both imaging techniques and processing provided novel insights into the interfacial behavior and characteristics of the papillae. FTIR allowed for visualization of a live clingfish and its contact with an imaging surface. Using this technique, we observed that the papillae were last to remain engaged with an imaging surface, even when suction was removed. The rate of detachment was slow, and thus, FTIR did not demonstrate the rate-dependent effect on the adhesive capabilities of the papillae. However, we were able to gain an understanding of the interfacial behavior of the papillae in a live specimen.

Our use of image processing made it possible to elucidate trends in the geometries of surface structures involved in adhesion. We were able to analyze the suction disc in a quantifiable manner, which made it possible to tease out geometric characteristics that might have otherwise been overlooked. These geometric attributes have significant implications on modes of attachment, other than suction, that are employed by the disc. The attachment of the suction disc therefore cannot be represented as purely suction-based, but rather a combination of attachment processes that are dependent on the disturbances they act to resist.

Using an image processing analytical tool, we reduced possible human biases that could otherwise be introduced in the quantification of the papillae characteristics. Our use of image processing allowed for a higher degree of accuracy and rapid quantifications of the surface structures, providing for a large-scale, in-depth analysis of patterns. We propose that the automation of image processing for biology will yield considerable insights into the mechanisms that may otherwise be overlooked due to the labor-intensive nature of quantification. This would be especially applicable in analyzing the adhesive structures and patterns of other organisms, for which understanding the surface geometries and distributions on a broad scale may yield considerable insights into attachment.

Our image processing tool can be improved by automating the conversion of the original micrographs to a single binary image. We can envision the further improvement of image processing procedures by implementing machine learning algorithms to detect surface structures. Use of such machine learning algorithms could be used to further quantify the suction disc to yield perhaps even more novel or nuanced findings with regard to surface patterns. The synthesis of computer science, biology, and materials science is a step in advancing our understanding and applications of biological adhesives.

Scaling Effects of Geometry for Biomimetic Applications. Our analysis allowed us to design a biomimetic papilla, based on the averages calculated across all five clingfish specimens. The biomimetic surface structures were experimentally most resistant to shear loads, in comparison to other surface textures. The biomimetic surface structures can be applied to improve adhesion for wet environments. This could, in the case of the suction disc, inspire biomimetic designs of a smart suction cup, which can attach to rough surfaces and under a range of frequencies of disturbances. Previous work has been performed to mimic the clingfish to engineer suction devices to attach onto rough surfaces.^{32,53} In the previous

work, the contributions of the papillae and extracellular cuticle were approximated as a soft sealing layer lining the disc margin. Engineered geometric structures analogous to the papillae could be coupled with soft sealing and suction to design a hierarchical and complex suction disc that can successfully adhere to irregular surfaces given highly variable external forces. Such geometric structures could therefore enhance the attachment of biomimetic suction discs by their contributions to hydrodynamic adhesion and wet friction. We can envision scaling the extent or geometries of these engineered papillae structures to tailor them to the application. The use of such bioinspired structures to improve adhesion to wet or submerged surfaces would advance the fields of underwater manipulation and locomotion in unstructured environments, in which attachment is critical to success.

Geometry of Surface Structures Convergent across Evolution. We compared the surface patterns of clingfish to tree frogs, which also adhere using hydrodynamic adhesion and exhibit similar geometric epithelial cells that are hierarchical in structure.^{54–56} The tree frog secretes a mucus to increase the viscosity of the fluid beneath its toe pads.⁵⁷ The structure of the toe pads leverages the viscous secretion to adhere and enable locomotion on inclined and vertical surfaces.^{12,58,59}

We found overlapping similarities in the geometric attributes between clingfish and tree frogs (Figure 8). The surface areas of the papillae of the clingfish were on average 2 orders

magnitude greater than those of the epithelial cells of tree frogs (Figure 8a). This finding suggests that tree frogs have a greater density of channels across their toe pads. However, we found that the width of the channels in the tree frogs and clingfish were of the same order of magnitude, despite the significant difference in surface areas of the pads.^{29,55,60} Overall, the width of the channel did not change across body size or species. We suggest that the width of the channel may be optimized for directing viscous secretions while mitigating the loss of surface area due to channeling. Fluid channeling would therefore reduce the distance of separation of the adhesive pad from a surface in both tree frogs and clingfish. This reduced distance would allow for the organisms to exploit normal adhesion due to hydrodynamic forces and would also increase the contribution of wet friction to help counteract dislodgement.

The overall distribution of shapes between the tree frog and clingfish is notably similar (Figure 8b). Most of the surface patterns for both species are hexagonal in shape, while the second most prevalent structure is pentagonal. The use of hexagonal structures in tree frogs is similar in role to its hypothesized function in clingfish. The hexagonal structure would be critical in densely packing an irregular surface, optimizing contact area and channel density. The hexagonal epithelial cells in both tree frogs and clingfish would therefore increase the frictional footprint of the organism when subjected to shear disturbances.

Tree frogs and clingfish express similar aspect ratios of their epithelial cells (1.47 for tree frogs, Chen et al.; 1.33 for clingfish; Figure 8d).²⁹ In frogs, the orientation of the elongated hexagons resists the shear loads experienced when climbing surfaces.²⁹ Therefore, the friction of the elongated toe pads in frogs is predominantly used to counteract the effect of gravity. For the clingfish, we concluded that the elongated papillae are used to reinforce the outer perimeter of the disc margin via friction. However, the clingfish is less affected by gravity, as experienced by tree frogs, and is rather subjected to intertidal forces that vary greatly in direction, frequency, and magnitude. The differences in environmental forces may account for the differences in orientations of the elongated epithelial cells between the tree frog and clingfish. The tree frog experiences predictable dislodgement forces, due to gravity, whereas the clingfish experiences unpredictable dislodgement forces, due to its intertidal habitat. However, the elongated epithelial cells would serve the same function of stabilizing the attachment of the organisms.

Overall, our comparison of the structure of the clingfish to the tree frog has reinforced our conclusions that the geometric properties of the papillae play considerable roles in adhesion. The noticeable similarities between tree frogs and clingfish lead us to propose a convergent evolution of their structures that leverage attachment due to hydrodynamic adhesion and friction.

CONCLUSIONS

The suction disc of the clingfish provides a model for bioinspired adhesion to wet, rough surfaces under nonuniform loading conditions. Our results suggest that the papillae function to seal the suction disc using hydrodynamic adhesion and wet friction during high-frequency disturbances. The automated characterization of surface structures made possible the visualization of spatial trends of papillae across the disc margin. Future work could use similar automated techniques to assess the geometric characteristics of other structured

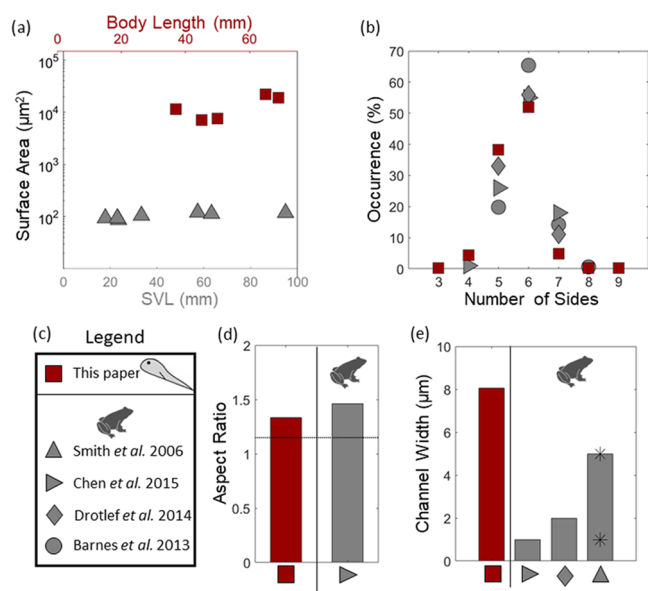


Figure 8. Geometric similarities between the toe pads of tree frogs and the suction disc of the clingfish. (a) Comparison of the surface areas of the individual epithelial protrusions between species. Tree frog data (gray triangle) from Smith et al.²⁵ Clingfish data represented as red squares. Body length (mm) of the clingfish was measured snout to tail. Snout–vent length (SVL) was reported for the body length of the tree frog, measured snout to anus. (b) Comparison of the occurrence of different shapes of the epithelial projections. Gray, right-pointing triangle, data from Chen et al.²⁹ Gray diamond, data from Drotlef et al.⁶⁰ Gray circle, data from Barnes et al.⁵⁵ (c) Legend denoting the symbols and referenced sources for the data presented in the subfigures. (d) Comparison of the aspect ratio of the papillae of clingfish and projections from the toe pads of tree frogs. (e) Comparison of the channel width (µm) between epithelial projections. The star indicates the maximum and minimum bounds of the data presented in Smith et al.²⁵

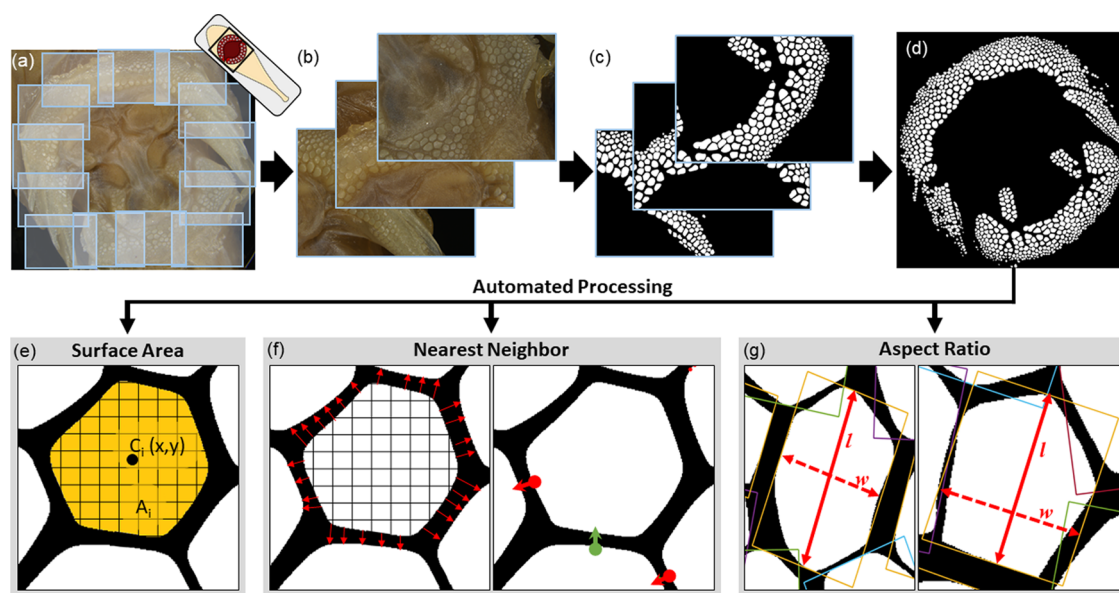


Figure 9. Methodology for the quantification of the papillae. (a) Overview of the imaging sequence. Images to overlap by 25%. (b) Example micrographs to be processed. (c) Individual papillae were outlined manually, creating a binary image of the original micrograph. (d) Binary images were stitched together at overlapping regions. (e) Image processing automatically detected and characterized the resulting binary image. Each papilla was considered by the program as a region of interest (ROI). Surface area was computed for every papilla as the sum of the pixels in the ROI. $C(x,y)$ denoted the center of the ROI, which served as an identifier and was used in future mapping functions. (f) Determination of the channel width by calculation of the nearest neighbor. (Left) For every papilla, each pixel along its perimeter was used to calculate its nearest neighbor. (Right) We averaged the five shortest distances to the nearest neighbor and considered that to be the minimum channel spacing of that individual papilla. The result of such computation is shown with red and green bold lines. The arrows point from the interrogated papilla to its nearest neighbor at the site with the smallest channel spacing. (g) Determination of the aspect ratio of each individual papilla. A bounding box was computed for each papilla, accounting for all vertices and the orientation of the ROI. The length (l) and width (w) of the box were used to compute the aspect ratio.

892 adhesives found in nature. An “average” papilla was computed
893 across all 4853 papillae surveyed in this study to be an
894 elongated hexagon, similar to that observed in the surface
895 structure of tree frogs.⁶⁰ The computed papilla was used to
896 design a biomimetic surface structure that could be used for
897 future applications in engineered wet adhesives.

898 ■ METHODS

899 **Biological Sample Preparation.** Two live clingfish (*G.*
900 *maeandricus*) were collected along the San Diego coastline under a
901 collection permit to accredited organisms’ collector, P. Zerofski
902 (Scripps Institution of Oceanography). Animal care protocol IACUC
903 #S11071 was issued to D. Deheyn. The live clingfish was imaged
904 using FTIR.

905 We collected the secretions of a live specimen for microrheological
906 analysis. The specimen was placed on a dry glass slide to reduce the
907 presence of seawater in the sample. A pipette was used to probe and
908 collect secretions at the intersection of the suction disc and the glass
909 slide. Between 10 and 20 μL of secretion were collected per sampling
910 period. Sampling occurred over 4 days with at least 12 h between
911 collection events. Secretions were stored at $-20\text{ }^\circ\text{C}$ prior to
912 microrheological analysis. Previous work indicated that storage up
913 to 30 days at $-20\text{ }^\circ\text{C}$ does not change the viscoelastic properties of
914 mucosal secretions.⁴⁸ To image the secretions, we placed and
915 removed a live clingfish on a dry glass slide. The secretions on the
916 glass slide were dried and imaged using an optical microscope
917 (Eclipse 50i, Nikon Co.).

918 We imaged the suction discs of the preserved clingfish (*G.*
919 *maeandricus*) specimen available from the Scripps Marine Vertebrate
920 Collection. Preserved specimens were collected from San Luis
921 Obispo, CA, and maintained in 50% isopropanol. We chose
922 specimens of five different body sizes for the same species. The
923 specimens were measured for body length from snout to tail and

weight both prior to imaging (Table S1). The diameter of the suction
924 disc was measured using ImageJ.⁶¹ 925

Frustrated Total Internal Reflection (FTIR). The setup for the
926 FTIR experiment was custom-built.⁴⁴ The imaging station consisted
927 of a 3D printed mount, 9.7 mm thick plate of acrylic, and natural
928 white light-emitting diode (LEDs) (3528-24VDC, Super Bright
929 LEDs, Inc.). Light from the diodes was internally reflected within the
930 acrylic, and contact with the imaging plate allowed for the
931 illumination of the suction disc. The acrylic was wetted with a thin
932 layer of seawater for all FTIR trials. The clingfish was placed on the
933 inverted imaging surface, which was imaged with a camera (1280 \times
934 780 pixels, 140 pixels/cm, 40 frames/second; EXILIM EX-FH25,
935 Casio Computer Co., Ltd.). Different components of the suction
936 chamber were isolated. Disruption of the suction disc was induced by
937 a gentle prodding with a blunt spatula at the intersection of the pelvic
938 and pectoral fins. 939

Passive Microrheology. For passive microrheology measure-
940 ments, a trace amount of 1 μm carboxylated polystyrene microspheres
941 (Polysciences, Inc.) was added to clingfish secretion. Beads were
942 coated with Alexa-488 bovine serum albumin (BSA) to minimize
943 adsorption and enable fluorescence visualization. This coating confers
944 a no-stick boundary condition between the beads and the surrounding
945 solution. Diffusing microspheres were visualized using an Olympus
946 IX73 microscope with a 20 \times objective and a high-speed
947 complementary metal-oxide-semiconductor (CMOS) camera (Ha-
948 mamatsu Orca Flash 2.8). For each sample, 10 time series of 1920 \times
949 1440 (181 nm/pixel) images consisting of ~ 50 beads/frame were
950 recorded for 20 s at 45 fps. A custom-written Python code was used to
951 extract the trajectories of diffusing beads and calculate the mean-
952 squared displacements (MSDs) in the x and y directions. MSDs
953 (Figure S6) shown consist of ~ 500 particles and are an average of
954 MSDs in the x and y directions, denoted as $\langle \Delta r^2(t) \rangle$. Linear
955 viscoelastic moduli ($G'(\omega)$, $G''(\omega)$) were determined via the
956 generalized Stokes–Einstein relation⁶² 957

$$G^*(\omega) = G'(\omega) + iG''(\omega) = \frac{k_B T}{i\omega \langle \Delta r^2(\omega) \rangle \pi R} \quad (4)$$

where k_B is Boltzmann's constant, T is the absolute temperature, $\langle \Delta r^2(\omega) \rangle$ is the Fourier transform of $\langle \Delta r^2(t) \rangle$, and R is the radius of the beads. The Fourier transform of $\langle \Delta r^2(t) \rangle$ is obtained by⁶³

$$-\omega^2 \langle \Delta r^2(\omega) \rangle = (1 - e^{-i\omega t_1}) \frac{\langle \Delta r^2(t_1) \rangle}{t_1} + 2D e^{-i\omega t_N} + \sum_{k=2}^N \left(\frac{\langle \Delta r^2(t_k) \rangle - \langle \Delta r^2(t_{k-1}) \rangle}{t_k - t_{k-1}} \right) (e^{-i\omega t_{k-1}} - e^{-i\omega t_k}) \quad (5)$$

where 1 and N in the equation represent the first and last points from the oversampled MSD data, respectively. Oversampling is done using the PCHIP MATLAB function. More details about the data analysis can be found in ref 64.

Preparation of Micrographs for Binary Image. Preserved specimens were imaged under brightfield microscopy (SMZ18 stereo microscope; DS-F13 Camera, Nikon) at a 2× magnification. We imaged the circumference of the disc with a 25% overlap of content in the micrographs (Figure 9a). The papillae in each micrograph were manually outlined in graphics software (Illustrator, Adobe Inc., 2019; Figure 9c). We used the vectorized outlines of the papillae to generate a binary image in which white regions represented individual papillae and black represented the background. All binary images of the micrographs were manually stitched together by orienting the overlapping regions (Figure 9d). The conversion of micrographs to binary images was performed for all five different body sizes of clingfish (sizes I–V).

To understand the trends in region properties across various parts of the suction disc, we also manually segmented the binary image for one suction disc (size V) into three components using a graphics software. We segmented the disc into three binary images containing one of the following: two rows of the outermost radius of the anterior and posterior regions of the disc, three rows nearest the innermost radius of the anterior and posterior, and the lateral fin regions of the suction disc.

Automated Region Detection of Papillae across Entire Disc. We developed an image processing sequence to automatically characterize the binary image of the clingfish suction disc (Figure 9). All image processing was performed in MATLAB (2018, The MathWorks, Inc.). The computer program labeled and characterized each papilla, which was labeled in the program as a region of interest (ROI). The regions of interest underwent a thresholding filter dictating that the area of each ROI must be larger than 20 pixels, to exclude noise present in the data. Each ROI was defined by a discrete boundary and was assigned a unique identity, where all pixels included within that region shared that identity.

Using image processing toolboxes native to MATLAB, we extracted region properties about each individual papilla, thereby calculating surface area (μm^2), perimeter (μm), and orientation of each papilla across the disc (Figure 9e). This region processing was performed on all clingfish body sizes (I–V), allowing for rapid characterization of the entire suction discs. The region processing code was also performed across all body segments for the size V segmentation study. All plots were generated using MATLAB.

Automated Characterization of the Area of Papillae. With the resulting data from our region detection procedure, trends in surface area were mapped based on ROI location to the original binary image. To understand the distribution of papillae based on size across this binary map, we normalized the surface area of an individual papilla (A_i) to that of the largest papilla (A_{max}) per suction disc (normalized area, $A_{\text{norm}} = A_i/A_{\text{max}}$). The binary map was converted into a heat map, where color was used to represent the normalized surface area. Such heat map provided insight into trends in the size of papillae along the suction disc.

Automated Characterization of Aspect Ratio. We automatically computed the aspect ratio of each ROI across the suction disc,

which represented the elongation of the papillae. This computation defined the minimal bounding rectangle around a set of points. A bounding box was computed to contain the major and minor axes and all vertices of the ROI (Figure 9g). The bounding box was rotated to the orientation of the ROI, and the aspect ratio (R_{aspect}) was calculated to be the ratio of the length (l) to width (w) of the bounding box ($R_{\text{aspect}} = l/w$).

Automated Characterization of Channel Width. We automated the calculation of the width of the channel formed between neighboring papillae. This computation calculated the shortest distance between ROIs. For each point along the perimeter of the ROI, the minimum distance to the neighboring ROI was computed, thus reporting the nearest neighbor of each point along the circumference of the ROI (Figure 9f). The program then averaged the five points along the circumference of the ROI that have the minimum distance to a neighboring ROI. The average of the minimum distance to a neighboring ROI was considered the minimum channel width per papillae. Only one averaged minimum distance was calculated per papilla. The calculation of channel width was performed across the entirety of the suction disc.

Manual Characterization of Papilla Shape. We manually characterized the shape of papillae across the disc margin of the largest clingfish, size V. We chose to manually count the number of sides of each papilla instead of automating its characterization. The finer edges of the papillae were smoothed in the process of vectorizing and compressing the binary image. This smoothing made it difficult for a computer program to be developed to resolve the finer edges and thus accurately count the number of sides. Therefore, we visually inspected the original brightfield micrographs and manually counted the number of sides of each papilla in the micrograph. We then labeled the corresponding papillae in the binary mask, tagging each ROI with different colors to indicate the number of sides of the individual. Papillae that were considered too damaged to discern the number of sides were labeled as deteriorated. We created a program to count the abundance of each labeled region based on color, thereby quantifying the prevalence of shapes across the suction disc.

Fabrication of the Biomimetic Surface Structures. We designed the biomimetic surface structure in a computer-aided design program (AutoCAD, Autodesk Inc.). We fabricated the mold of the surface structures by engraving the designs into acrylic using a laser machining system (PLS6MW, Universal Laser Systems). The surface patterns were either elongated hexagons (aspect ratio, 1.3), regular hexagons, or squares, all of the same surface area, 0.21 mm^2 . The channel spacing between the surface structures was $150 \mu\text{m}$. The total footprint of the surface texture was $30 \text{ mm} \times 30 \text{ mm}$.

We prepared the silicone (Young's modulus, 1.1 MPa; Dragon Skin 20, Smooth-On, Inc.) with a blue silicone pigment (Silc Pig, Smooth-On, Inc.) for better visualization. We degassed the silicone in a vacuum chamber for 5 min and poured the mixture into the molds. The molds were then degassed for 15 min to prevent the accumulation of bubbles in the microscale features of the surface textures. We partially cured the silicone for 5 min at $45 \text{ }^\circ\text{C}$. We applied a stiff backing composed of acrylic ($30 \text{ mm} \times 30 \text{ mm}$) to the surface texture. A silicone adhesive (0.5 mm thickness; ARclad IS-7876; Adhesives Research, Inc.) provided the interface between the acrylic and the silicone mold. The assembly was then fully cured.

To prepare for the test of shear stress, we applied an inextensible nylon cord (25 cm length) to the back of the acrylic using cyanoacrylate adhesive (Loctite Super Glue Gel, Henkel Corporation).

Testing Performance of the Biomimetic Surface Structures. We experimentally tested the effect of the surface structures on resistance to shear dislodgement forces. We performed these experiments on a mechanical testing system outfitted with a force gauge of a maximum force and a resolution of 100 and 0.02 N, respectively (M7-20, Mark-10 Co.). Shear tests were conducted using a motorized test stand (ESM303, Mark-10 Co.) at a speed of retraction of 50 mm/min .

The inextensible cord stemming from the acrylic backing of the surface structure was routed through a frictionless pulley to the upper

1089 clamp of the motorized stage. The surface on which the test was
1090 performed was composed of smooth acrylic and lubricated with
1091 glycerol (viscosity, 1.4 Pa·s; Vegetable Glycerin, Essential Depot,
1092 Co.). A preload of 200 g was applied to the acrylic backing. Shear tests
1093 were initiated upon retraction of the upper clamp. The force reported
1094 in the shear stress was determined to be the steady-state value of force
1095 across the duration of the test. The force was normalized to the total
1096 surface area and reported as shear stress (kPa). Experiments were
1097 performed in triplicate.

1098 ■ ASSOCIATED CONTENT

1099 ■ Supporting Information

1100 The Supporting Information is available free of charge at
1101 <https://pubs.acs.org/doi/10.1021/acsami.0c10749>.

1102 Suction disc diameter corresponded to body size and
1103 was dependent on the state of preservation (Figure S1);
1104 surface area of papillae across all body sizes (Figure S2);
1105 example of large papillae in Chilean clingfish (Figure
1106 S3); aspect ratio of papillae across all body sizes (Figure
1107 S4); binary maps of papillae based on the number of
1108 sides (Figure S5); mean-squared displacements (MSDs)
1109 of diffusing beads in clingfish secretion (Figure S6);
1110 demonstration of the image processing protocol for size
1111 V (Figure S7); sizes and weights of the clingfish
1112 specimen (Table S1); and computed values of geometric
1113 attributes of papillae (Table S2) (PDF)

1114 ■ AUTHOR INFORMATION

1115 Corresponding Authors

1116 **Jessica A. Sandoval** – *Materials Science and Engineering*
1117 *Program, Department of Mechanical and Aerospace*
1118 *Engineering, University of California, San Diego, La Jolla,*
1119 *California 92093, United States*; [orcid.org/0000-0002-](https://orcid.org/0000-0002-7598-8135)
1120 [7598-8135](https://orcid.org/0000-0002-7598-8135); Email: jas164@eng.ucsd.edu

1121 **Dimitri D. Deheyn** – *Marine Biology Research Division, Scripps*
1122 *Institution of Oceanography, La Jolla, California 92093, United*
1123 *States*; Email: ddeheyn@ucsd.edu

1124 Authors

1125 **Jade Sommers** – *Department of Mechanical Engineering, San*
1126 *Diego State University, San Diego, California 92182, United*
1127 *States*

1128 **Karthik R. Peddireddy** – *Department of Physics and*
1129 *Biophysics, University of San Diego, San Diego, California*
1130 *92110, United States*; orcid.org/0000-0003-4282-5484

1131 **Rae M. Robertson-Anderson** – *Department of Physics and*
1132 *Biophysics, University of San Diego, San Diego, California*
1133 *92110, United States*; orcid.org/0000-0000-4475-4667

1134 **Michael T. Tolley** – *Materials Science and Engineering*
1135 *Program, Department of Mechanical and Aerospace Engineering*
1136 *and Department of Mechanical and Aerospace Engineering,*
1137 *University of California, San Diego, La Jolla, California 92093,*
1138 *United States*

1139 Complete contact information is available at:
1140 <https://pubs.acs.org/doi/10.1021/acsami.0c10749>

1141 Author Contributions

1142 J.A.S., D.D.D., and M.T.T. conceived the project. M.T.T.
1143 provided guidance on the technical and engineering aspects,
1144 while D.D.D. provided guidance on the biological components.
1145 R.M.R.-A. provided guidance on microrheological character-
1146 izations. J.A.S. performed FTIR experiments on live clingfish.
1147 J.A.S. imaged the preserved specimen and performed the

1148 manual binary conversions of the micrographs. J.A.S. 1148
1149 programmed the automation procedures to quantify the 1149
1150 papillae. K.R.P. performed the microrheological experiments 1150
1151 and analysis. J.A.S. performed the mathematical modeling of 1151
1152 the papillae and comparisons to tree frogs. J.A.S. designed, 1152
1153 fabricated, and tested the biomimetic surface textures. J.A.S. 1153
1154 prepared the initial draft of the manuscript, and all authors 1154
1155 provided feedback during revisions. 1155

1156 Funding

1157 This work is supported by the Office of Naval Research (Grant 1157
1158 no. N000141712062) and the Air Force Office of Scientific 1158
1159 Research (Grant no. AFOSR-FA9550-17-1-0249). J.A.S. is 1159
1160 supported by the Gates Millennium Scholars (GMS) Program. 1160

1161 Notes

1162 The authors declare no competing financial interest. 1162
1163 Please contact J.A.S. for data and other materials. 1163

1164 ■ ACKNOWLEDGMENTS

1165 We thank the Scripps Marine Vertebrate Collection for the 1165
1166 generous use of their preserved clingfish specimen. We thank 1166
1167 K. Wood (SDSU) for the guidance of J.S. We thank N. Gravish 1167
1168 (UCSD) for the use of the FTIR imaging station. This work 1168
1169 was facilitated by the Biomimicry for Emerging Science and 1169
1170 Technology (BEST) Initiative and the Bioinspired Robotics 1170
1171 and Design Lab (BRDL). 1171

1172 ■ REFERENCES

- 1173 (1) Favi, P. M.; Yi, S.; Lenaghan, S. C.; Xia, L.; Zhang, M. 1173
1174 Inspiration from the Natural World: From Bio-Adhesives to Bio- 1174
1175 Inspired Adhesives. *J. Adhes. Sci. Technol.* **2014**, *28*, 290–319. 1175
- 1176 (2) Peattie, A. M. Functional Demands of Dynamic Biological 1176
1177 Adhesion: An Integrative Approach. *J. Comp. Physiol., B* **2009**, *179*, 1177
1178 231–239. 1178
- 1179 (3) Gorb, S. N. Biological Attachment Devices: Exploring Nature's 1179
1180 Diversity for Biomimetics. *Philos. Trans. R. Soc., A* **2008**, *366*, 1557– 1180
1181 1574. 1181
- 1182 (4) Shintake, J.; Cacucciolo, V.; Floreano, D.; Shea, H. Soft Robotic 1182
1183 Grippers. *Adv. Mater.* **2018**, *30*, No. 1707035. 1183
- 1184 (5) Cutkosky, M. R. Climbing with Adhesion: From Bioinspiration 1184
1185 to Biounderstanding. *Interface Focus* **2015**, *5*, No. 20150015. 1185
- 1186 (6) Chattopadhyay, P.; Ghoshal, S. K. Adhesion Technologies of 1186
1187 Bio-Inspired Climbing Robots: A Survey. *Int. J. Rob. Autom.* **2018**, *33*, 1187
1188 654–661. 1188
- 1189 (7) Sameoto, D.; Menon, C. Recent Advances in the Fabrication and 1189
1190 Adhesion Testing of Biomimetic Dry Adhesives. *Smart Mater. Struct.* 1190
1191 **2010**, *19*, No. 103001. 1191
- 1192 (8) Endlein, T.; Barnes, W. J. P. Wet Adhesion in Tree and Torrent 1192
1193 Frogs. *Encyclopedia of Nanotechnology*; Springer: Netherlands, 2015; 1193
1194 pp 4355–4373. 1194
- 1195 (9) Meng, F.; Liu, Q.; Wang, X.; Tan, D.; Xue, L.; Barnes, W. J. P. 1195
1196 Tree Frog Adhesion Biomimetics: Opportunities for the Development 1196
1197 of New, Smart Adhesives That Adhere under Wet Conditions. *Philos.* 1197
1198 *Trans. R. Soc., A* **2019**, *377*, No. 20190131. 1198
- 1199 (10) Butt, H. J.; Barnes, W. J. P.; Del Campo, A.; Kappl, M.; 1199
1200 Schönfeld, F. Capillary Forces between Soft, Elastic Spheres. *Soft* 1200
1201 *Matter* **2010**, *6*, 5930–5936. 1201
- 1202 (11) Barnes, W. J. P. Adhesion in Wet Environments: Frogs. In 1202
1203 *Encyclopedia of Nanotechnology*; Bhushan, B., Ed.; Springer: Nether- 1203
1204 lands, Dordrecht, 2012; pp 70–83. 1204
- 1205 (12) Langowski, J. K. A.; Dodou, D.; Kamperman, M.; van Leeuwen, 1205
1206 J. L. Tree Frog Attachment: Mechanisms, Challenges, and 1206
1207 Perspectives. *Front. Zool.* **2018**, *15*, No. 32. 1207
- 1208 (13) Dirks, J. H. Physical Principles of Fluid-Mediated Insect 1208
1209 Attachment - Shouldn't Insects Slip? *Beilstein J. Nanotechnol.* **2014**, *5*, 1209
1210 1160–1166. 1210

- 1211 (14) Federle, W.; Riehle, M.; Curtis, A. S. G.; Full, R. J. An
1212 Integrative Study of Insect Adhesion: Mechanics and Wet Adhesion
1213 of Pretarsal Pads in Ants. *Integr. Comp. Biol.* **2002**, *42*, 1100–1106.
- 1214 (15) Amarपुरi, G.; Zhang, C.; Diaz, C.; Opell, B. D.; Blackledge, T.
1215 A.; Dhinojwala, A. Spiders Tune Glue Viscosity to Maximize
1216 Adhesion. *ACS Nano* **2015**, *9*, 11472–11478.
- 1217 (16) Shin, D.; Choi, W. T.; Lin, H.; Qu, Z.; Breedveld, V.; Meredith,
1218 J. C. Humidity-Tolerant Rate-Dependent Capillary Viscous Adhesion
1219 of Bee-Collected Pollen Fluids. *Nat. Commun.* **2019**, *10*, No. 1379.
- 1220 (17) Ditsche, P.; Summers, A. P. Aquatic versus Terrestrial
1221 Attachment: Water Makes a Difference. *Beilstein J. Nanotechnol.*
1222 **2014**, *5*, 2424–2439.
- 1223 (18) Li, X.; Tao, D.; Lu, H.; Bai, P.; Liu, Z.; Ma, L.; Meng, Y.; Tian,
1224 Y. Recent Developments in Gecko-Inspired Dry Adhesive Surfaces
1225 from Fabrication to Application. *Surf. Topogr.: Metrol. Prop.* **2019**, *7*,
1226 No. 023001.
- 1227 (19) Wainwright, D. K.; Kleinteich, T.; Kleinteich, A.; Gorb, S. N.;
1228 Summers, A. P. Stick Tight: Suction Adhesion on Irregular Surfaces in
1229 the Northern Clingfish. *Biol. Lett.* **2013**, *9*, No. 20130234.
- 1230 (20) Murphy, M. P.; Kim, S.; Sitti, M. Enhanced Adhesion by
1231 Gecko-Inspired Hierarchical Fibrillar Adhesives. *ACS Appl. Mater.*
1232 *Interfaces* **2009**, *1*, 849–855.
- 1233 (21) Lee, H.; Lee, B. P.; Messersmith, P. B. A Reversible Wet/Dry
1234 Adhesive Inspired by Mussels and Geckos. *Nature* **2007**, *448*, 338–
1235 341.
- 1236 (22) Yi, H.; Lee, S. H.; Seong, M.; Kwak, M. K.; Jeong, H. E.
1237 Bioinspired Reversible Hydrogel Adhesives for Wet and Underwater
1238 Surfaces. *J. Mater. Chem. B* **2018**, *6*, 8064–8070.
- 1239 (23) Wang, Y.; Kang, V.; Arzt, E.; Federle, W.; Hensel, R. Strong
1240 Wet and Dry Adhesion by Cupped Microstructures. *ACS Appl. Mater.*
1241 *Interfaces* **2019**, *11*, 26483–26490.
- 1242 (24) Cui, M.; Ren, S.; Wei, S.; Sun, C.; Zhong, C. Natural and Bio-
1243 Inspired Underwater Adhesives: Current Progress and New
1244 Perspectives. *APL Mater.* **2017**, *5*, No. 116102.
- 1245 (25) Smith, J. M.; Barnes, W. J. P.; Downie, J. R.; Ruxton, G. D.
1246 Structural Correlates of Increased Adhesive Efficiency with Adult Size
1247 in the Toe Pads of Hylid Tree Frogs. *J. Comp. Physiol., A* **2006**, *192*,
1248 1193–1204.
- 1249 (26) Glick, P.; Suresh, S. A.; Ruffatto, D.; Cutkosky, M.; Tolley, M.
1250 T.; Parness, A. A Soft Robotic Gripper with Gecko-Inspired Adhesive.
1251 *IEEE Rob. Autom. Lett.* **2018**, *3*, 903–910.
- 1252 (27) Jiang, H.; Hawkes, E. W.; Fuller, C.; Estrada, M. A.; Suresh, S.
1253 A.; Abcouwer, N.; Han, A. K.; Wang, S.; Ploch, C. J.; Parness, A.;
1254 Cutkosky, M. R. A Robotic Device Using Gecko-Inspired Adhesives
1255 Can Grasp and Manipulate Large Objects in Microgravity. *Sci. Rob.*
1256 **2017**, *2*, No. ean4545.
- 1257 (28) Kim, S.; Spenko, M.; Trujillo, S.; Heyneman, B.; Santos, D.;
1258 Cutkosky, M. R. Smooth Vertical Surface Climbing with Directional
1259 Adhesion. *IEEE Trans. Rob.* **2008**, *24*, 65–74.
- 1260 (29) Chen, H.; Zhang, L.; Zhang, D.; Zhang, P.; Han, Z. Bioinspired
1261 Surface for Surgical Graspers Based on the Strong Wet Friction of
1262 Tree Frog Toe Pads. *ACS Appl. Mater. Interfaces* **2015**, *7*, 13987–
1263 13995.
- 1264 (30) Wang, Y.; Yang, X.; Chen, Y.; Wainwright, D. K.; Kenaley, C.
1265 P.; Gong, Z.; Liu, Z.; Liu, H.; Guan, J.; Wang, T.; Weaver, J. C.;
1266 Wood, R. J.; Wen, L. A Biorobotic Adhesive Disc for Underwater
1267 Hitchhiking Inspired by the Remora Suckerfish. *Sci. Rob.* **2017**, *2*,
1268 No. ean8072.
- 1269 (31) Lee, S. H.; Song, H. W.; Kang, B. S.; Kwak, M. K. Remora-
1270 Inspired Reversible Adhesive for Underwater Applications. *ACS Appl.*
1271 *Mater. Interfaces* **2019**, *11*, 47571–47576.
- 1272 (32) Sandoval, J. A.; Jadhav, S.; Quan, H.; Deheyn, D. D.; Tolley, M.
1273 T. Reversible Adhesion to Rough Surfaces Both in and out of Water,
1274 Inspired by the Clingfish Suction Disc. *Bioinspiration Biomimetics*
1275 **2019**, *14*, No. 066016.
- 1276 (33) Santos, R.; Gorb, S.; Jamar, V.; Flammang, P. Adhesion of
1277 Echinoderm Tube Feet to Rough Surfaces. *J. Exp. Biol.* **2005**, *208*,
1278 2555–2567.
- (34) Sareh, S.; Althoefer, K.; Li, M.; Noh, Y.; Tramacere, F.; Sareh,
P.; Mazzolai, B.; Kovac, M. Anchoring like Octopus: Biologically
Inspired Soft Artificial Sucker. *J. R. Soc. Interface* **2017**, *14*,
No. 20170395.
- (35) Greco, G.; Bosia, F.; Tramacere, F.; Mazzolai, B.; Pugno, N. M.
The Role of Hairs in the Adhesion of Octopus Suckers: A
Hierarchical Peeling Approach. *Bioinspiration Biomimetics* **2020**, *15*,
No. 035006.
- (36) Lin, A. Y. M.; Brunner, R.; Chen, P. Y.; Talke, F. E.; Meyers, M.
A. Underwater Adhesion of Abalone: The Role of van Der Waals and
Capillary Forces. *Acta Mater.* **2009**, *57*, 4178–4185.
- (37) Britz, R.; Johnson, G. D. Ontogeny and Homology of the
Skeletal Elements That Form the Sucking Disc of Remoras (Teleostei,
Echeneoidei, Echeneidae). *J. Morphol.* **2012**, *273*, 1353–1366.
- (38) Das, D.; Nag, T. C. Adhesion by Paired Pectoral and Pelvic
Fins in a Mountain-Stream Catfish, *Pseudocheneis sulcatus* (Sisoridae).
Environ. Biol. Fishes **2004**, *71*, 1–5.
- (39) De Crop, W.; Pauwels, E.; Van Hoorebeke, L.; Geerinckx, T.
Functional Morphology of the Andean Climbing Catfishes (Astro-
blepidae, Siluriformes): Alternative Ways of Respiration, Adhesion,
and Locomotion Using the Mouth. *J. Morphol.* **2013**, *274*, 1164–
1179.
- (40) Chuang, Y. C.; Chang, H. K.; Liu, G. L.; Chen, P. Y. Climbing
Upstream: Multi-Scale Structural Characterization and Underwater
Adhesion of the Pulin River Loach (*Sinogastromyzon puliensis*). *J.*
Mech. Behav. Biomed. Mater. **2017**, *73*, 76–85.
- (41) Green, D. M.; Barber, D. L. The Ventral Adhesive Disc of the
Clingfish *Gobiesox maeandricus*: Integumental Structure and Adhesive
Mechanisms. *Can. J. Zool.* **1988**, *66*, 1610–1619.
- (42) Ditsche, P.; Wainwright, D. K.; Summers, A. P. Attachment to
Challenging Substrates - Fouling, Roughness and Limits of Adhesion
in the Northern Clingfish (*Gobiesox maeandricus*). *J. Exp. Biol.* **2014**,
217, 2548–2554.
- (43) Kuruvilla, J.; Sukumaran, D.; Sankar, A.; Joy, S. P. In *A Review*
on Image Processing and Image Segmentation, 2016 International
Conference on Data Mining and Advanced Computing (SAPIENCE),
2016; pp 198–203.
- (44) Han, J. Y. In *Low-Cost Multi-Touch Sensing through Frustrated*
Total Internal Reflection, Proceedings of the 18th Annual ACM
Symposium on User Interface Software and Technology, 2005; pp
115–118.
- (45) White, C. R.; Seymour, R. S. Mammalian Basal Metabolic Rate
Is Proportional to Body Mass^{2/3}. *Proc. Natl. Acad. Sci. U.S.A.* **2003**,
100, 4046–4049.
- (46) Menárguez, M.; Pastor, L. M.; Odebad, E. Morphological
Characterization of Different Human Cervical Mucus Types Using
Light and Scanning Electron Microscopy. *Hum. Reprod.* **2003**, *18*,
1782–1789.
- (47) Cortés, M. E.; González, F.; Vigil, P. Crystallization of Bovine
Cervical Mucus at Oestrus: An Update. *Rev. Med. Vet.* **2014**, *28*, 103–
116.
- (48) Lai, S. K.; Wang, Y. Y.; Wirtz, D.; Hanes, J. Micro- and
Macrorheology of Mucus. *Adv. Drug Delivery Rev.* **2009**, *61*, 86–100.
- (49) Ditsche, P.; Hicks, M.; Truong, L.; Linkem, C.; Summers, A.
From Smooth to Rough, from Water to Air: The Intertidal Habitat of
Northern Clingfish (*Gobiesox maeandricus*). *Sci. Nat.* **2017**, *104*,
No. 33.
- (50) Nagpal, R.; Patel, A.; Gibson, M. C. Epithelial Topology.
BioEssays **2008**, *30*, 260–266.
- (51) Chung, J. Y.; Chaudhury, M. K. Roles of Discontinuities in Bio-
Inspired Adhesive Pads. *J. R. Soc. Interface* **2005**, *2*, 55–61.
- (52) Leroy, S.; Charlaix, E. Hydrodynamic Interactions for the
Measurement of Thin Film Elastic Properties. *J. Fluid Mech.* **2011**,
674, 389–407.
- (53) Ditsche, P.; Summers, A. Learning from Northern Clingfish (*Gobiesox maeandricus*): Bioinspired Suction Cups Attach to Rough
Surfaces. *Philos. Trans. R. Soc., B* **2019**, *374*, No. 20190204.

- 1346 (54) Green, D. M. Treefrog Toe Pads: Comparative Surface
1347 Morphology Using Scanning Electron Microscopy. *Can. J. Zool.* **1979**,
1348 *57*, 2033–2046.
- 1349 (55) Barnes, W. J. P.; Baum, M.; Peisker, H.; Gorb, S. N.
1350 Comparative Cryo-SEM and AFM Studies of Hylid and Rhacophorid
1351 Tree Frog Toe Pads. *J. Morphol.* **2013**, *274*, 1384–1396.
- 1352 (56) Hanna, G.; Jon, W.; Barnes, W. J. P. Adhesion and Detachment
1353 of the Toe Pads of Tree Frogs. *J. Exp. Biol.* **1991**, *155*, 103–125.
- 1354 (57) Federle, W.; Barnes, W. J. P.; Baumgartner, W.; Drechsler, P.;
1355 Smith, J. M. Wet but Not Slippery: Boundary Friction in Tree Frog
1356 Adhesive Toe Pads. *J. R. Soc. Interface* **2006**, *3*, 689–697.
- 1357 (58) Endlein, T.; Barnes, W. J. P.; Samuel, D. S.; Crawford, N. A.;
1358 Biaw, A. B.; Grafe, U. Sticking under Wet Conditions: The
1359 Remarkable Attachment Abilities of the Torrent Frog, *Staurois*
1360 *Guttatus*. *PLoS One* **2013**, *8*, No. e73810.
- 1361 (59) Hill, I. D. C.; Dong, B.; Barnes, W. J. P.; Ji, A.; Endlein, T. The
1362 Biomechanics of Tree Frogs Climbing Curved Surfaces: A Gripping
1363 Problem. *J. Exp. Biol.* **2018**, *221*, No. jeb168179.
- 1364 (60) Drotlef, D. M.; Appel, E.; Peisker, H.; Dening, K.; del Campo,
1365 A.; Gorb, S. N.; Barnes, W. J. P. Morphological Studies of the Toe
1366 Pads of the Rock Frog, *Staurois parvus* (Family: Ranidae) and Their
1367 Relevance to the Development of New Biomimetically Inspired
1368 Reversible Adhesives. *Interface Focus* **2014**, *5*, No. 20140036.
- 1369 (61) Schneider, C. A.; Rasband, W. S.; Eliceiri, K. W. NIH Image to
1370 ImageJ: 25 Years of Image Analysis. *Nat. Methods* **2012**, *9*, 671–675.
- 1371 (62) Mason, T. G.; Dhople, A.; Wirtz, D. Linear Viscoelastic Moduli
1372 of Concentrated DNA Solutions. *Macromolecules* **1998**, *31*, 3600–
1373 3603.
- 1374 (63) Evans, R. M. L.; Tassieri, M.; Auhl, D.; Waigh, T. A. Direct
1375 Conversion of Rheological Compliance Measurements into Storage
1376 and Loss Moduli. *Phys. Rev. E: Stat., Nonlinear, Soft Matter Phys.* **2009**,
1377 *80*, No. 012501.
- 1378 (64) Tassieri, M.; Evans, R. M. L.; Warren, R. L.; Bailey, N. J.;
1379 Cooper, J. M. Microrheology with Optical Tweezers: Data Analysis.
1380 *New J. Phys.* **2012**, *14*, No. 115032.
- 1381 (65) D'Errico, J. A suite of minimal bounding objects (MATLAB
1382 FileExchange), 2019. [https://www.mathworks.com/matlabcentral/
1383 fileexchange/34767-a-suite-of-minimal-bounding-objects](https://www.mathworks.com/matlabcentral/fileexchange/34767-a-suite-of-minimal-bounding-objects) (accessed
1384 Aug, 2019).
- 1385 (66) Fricker, P. getNearestNeighborDistances.m (MATLAB Fil-
1386 eExchange), 2019. [https://www.mathworks.com/matlabcentral/
1387 fileexchange/47964-getnearestneighbordistances-m](https://www.mathworks.com/matlabcentral/fileexchange/47964-getnearestneighbordistances-m) (accessed Aug,
1388 2019).
- 1389 (67) Yap, H. K.; Goh, J. C. H.; Yeow, R. C. H. Design and
1390 Characterization of Soft Actuator for Hand Rehabilitation Applica-
1391 tion. *IFMBE Proc.* **2015**, *45*, 367–370.